Bidirectional control of goal-oriented action selection by distinct prefrontal cortex circuits

Rafiq Huda[1], Grayson O. Sipe[1], Elie Adam[1], Vincent Breton-Provencher[1], Gerald N. Pho[1], Liadan M. Gunter[1], Ian R. Wickersham[2] & Mriganka Sur[1,3,*]

[1]Picower Institute for Learning and Memory
Department of Brain and Cognitive Sciences
Massachusetts Institute of Technology, Cambridge, MA 02139, USA.

[2]McGovern Institute for Brain Research
Massachusetts Institute of Technology, Cambridge, MA 02139, USA.

[3]Lead contact

*Correspondence: msur@mit.edu

Summary

The immense behavioral repertoire of animals necessitates mechanisms that select and suppress specific actions depending on current goals. The prefrontal cortex (PFC) has been suggested to orchestrate these processes by biasing activity in its target structures, but how its vastly converging inputs and diverging outputs are coordinated to control goal-oriented actions remains unclear. Here we use a bilateral task in which mice select between symmetric but opposing actions to show that distinct outputs from a subdivision of the PFC, the anterior cingulate cortex (ACC), promote correct and suppress incorrect actions. Surprisingly, ACC outputs to the superior colliculus principally inhibit incorrect actions. Optogenetic analyses and a projection-based activity model make the unexpected prediction that feedback from the ACC to the visual cortex promotes correct actions, which we confirm. Our results show that anatomically non-overlapping but functionally complementary PFC outputs bidirectionally control actions, and suggest a candidate organizing principle for PFC circuits.

Keywords

Prefrontal cortex, action selection, superior colliculus, visual cortex

Introduction

Animals respond to their environments using complex and diverse motor movements, but are limited by being able to enact only single actions at a time. Hence, voluntary control over behavior requires context-dependent mechanisms that promote appropriate actions and suppress complementary but inappropriate ones. Such bidirectional control of action is readily apparent in sets of commonly displayed opposing behaviors, such as freeze/flight, approach/avoidance, and exploration/exploitation (Blanchard et al., 2001; Fadok et al., 2017; Frank et al., 2009; Hardung et al., 2017; Humphries et al., 2012; Shenhav et al., 2016). An emerging theme from recent studies is that specific prefrontal cortex (PFC) circuits bidirectionally modulate the expression of innate behaviors such as conditioned fear responses (Bukalo et al., 2015; Rozeske et al., 2018), reward-seeking (Ferenczi et al., 2016; Kim et al., 2017; Otis et al., 2017), and social interactions (Murugan et al., 2017). The behavioral repertoire of animals is highly enriched by their ability to learn how to respond to environmental sensory cues with appropriate actions to achieve specific goals such as reward (Britten et al., 1992; Burgess et al., 2017; Erlich et al., 2011; Felsen and Mainen, 2008; Goard et al., 2016; Harvey et al., 2012; Li et al., 2015; Pinto and Dan, 2015; Raposo et al., 2014; Sanders and Kepecs, 2012). Such goal-oriented actions are at the core of a wide range of cognitive processes such as attention and response inhibition, and similarly require bidirectional control (Cisek and Kalaska, 2010; Miller and Cohen, 2001; Munoz and Everling, 2004). Unlike bidirectional modulation of innate behaviors that often consist of asymmetric action-inaction pairs (Murugan et al., 2017; Otis et al., 2017; Ye et al., 2016), animals can be trained to select from symmetrical pairs of actions such that the expression of each has a counter action that was suppressed, making sensory-guided action selection an attractive model for studying bidirectional control of behavior. Although the PFC has been widely implicated in the goal-oriented control of actions by modulating activity in downstream structures (Cohen et al., 2007; Gregoriou et al., 2012; Grunfeld and Likhtik, 2018; Miller and Cohen, 2001; Moore and Fallah, 2001; White et al., 2018; Wimmer et al., 2015; Zhang et al., 2014), a fundamental outstanding question is how the anatomical organization of inputs to and outputs from the PFC enables its proposed role in bidirectional control. Specifically, the circuit-level mechanisms by which the PFC transforms and integrates sensory inputs to generate top-down signals that differentially regulate downstream structures have remained unclear. Here, we use a combination of virus-mediated anatomical tracing, two-photon imaging of inputs/outputs, and projection-specific optogenetics to show that a

subdivision of the mouse PFC, the anterior cingulate cortex (ACC), uses distinct projection neuron populations to organize behaviors by promoting correct and suppressing incorrect actions.

Results

Prefrontal outputs select correct and suppress incorrect actions

To test the role of specific prefrontal circuits in top-down control of actions, we designed a task, modified from a previous design (Sanders and Kepecs, 2012), that required head-fixed mice to respond to the spatial location of a visual cue with one of two symmetric actions to earn water rewards. We trained mice to simultaneously learn two novel forepaw movements so that no particular action is reflexive and optimal performance requires expression of the correct (i.e., rewarded) and suppression of the incorrect action. Mice had to move a visual cue presented in either the left or right hemifield to the center by rotating a trackball fixed along a single axis (Figure 1A, B). Trials in which the cue was moved to the center were considered correct and rewarded, whereas trials in which the trackball was rotated in the direction opposite to that instructed by the cue were considered incorrect and not rewarded. We used a reaction time task-design that allowed mice to move as soon as they could after stimulus onset. This minimized potential confounds of short-term memory and extensive movement planning associated with delay tasks (Svoboda and Li, 2018). We first tested trained mice with stimuli of varying luminance and found that behavioral performance was dependent on stimulus strength (Figure S1A). We increased task difficulty further by simultaneously presenting two visual cues with different luminance intensities and requiring mice to respond to the cue with the higher luminance. We found that performance was perceptually limited by the difference in luminance of the two stimuli (Figure S1B). Hence, we presented single, high-luminance cues to minimize the effect of perceptual ambiguity on action control. Experienced mice performed well on this task (~90% accuracy), moving the ball rapidly at short latencies (~200ms) after stimulus onset (Figure S1C-G).

The motor-related intermediate and deep layers of the superior colliculus (SC_m) have been widely implicated in the expression of directional actions in many species, including in rodents (Dean et al., 1988; Felsen and Mainen, 2008; Krauzlis et al., 2013; Robinson, 1972; Schiller et al., 1987; Stubblefield et al., 2013; Wolf et al., 2015). Specifically, each hemisphere of SC_m coordinates actions to sensory cues in the contralateral hemifield, suggesting that in our task SC_m

may be necessary for the action that brings the contralateral cue to the center of the screen (contra action). We tested this by virally delivering the inhibitory optogenetic actuator Jaws (Chuong et al., 2014) in one hemisphere of SC_m and delivering yellow light (593 nm) through an optic fiber on a randomly selected subset of trials. Illuminating SC_m (or the cortex) with yellow (or blue) light in the absence of an opsin did not produce significant changes in behavior (Figure S2). Importantly, unilateral photoinhibition of SC_m did not grossly inhibit motor function, as there was no change in the miss rate (i.e., incomplete trials in which the ball is not moved to threshold), the movement velocity or start time for either action (Figure S3A). Instead, it selectively decreased the expression of contra actions regardless of whether they were the correct (i.e., cued by the stimulus) or the incorrect response. Hence, activity in SC_m plays a crucial role in the expression of contra actions. This raises the possibility that specific top-down PFC circuits increase activity in SC_m to promote contra actions when they are the correct response and decrease its activity to suppress such actions when they are incorrect.

To test this idea, we first used rabies virus-mediated retrograde tracing to identify sources of extrinsic inputs from the PFC to SC_m in mice. We found a high density of back-labeled neurons in the secondary motor and prefrontal cortex ipsilateral to the site of injection in SC_m (Figure S4A-H). We were particularly interested in the labeling observed in the medial PFC (corresponding to the anterior cingulate cortex, ACC) since recent studies suggest it to be a critical anatomical node in an extended cortico-subcortical network for guiding visual behaviors (Koike et al., 2016; Leinweber et al., 2017; White et al., 2018; Zhang et al., 2016; Zhang et al., 2014). Interestingly, SC-projecting neurons were located predominantly in the caudal ACC subdivision, suggesting anatomical specialization within the ACC along the caudo-rostral axis (Figures 1D; S4I). Hence, we focused our studies on the caudal ACC and assessed the contribution of its distinct top-down outputs to the bidirectional control of goal-oriented actions.

Given that activity in SC_m is necessary for the expression of contra actions (Figure 1C), we reasoned that if ACC outputs to SC_m facilitate performance by promoting correct actions, then inactivating these outputs will decrease the expression of contra actions (Figure 1E, model 1). In contrast, if these outputs promote goal-oriented behavior predominantly by suppressing incorrect contra actions, then inactivating them will lead to an increase in erroneous contra actions when the cue instructs an ipsi movement (Figure 1E, model 2). We distinguished between these possibilities by virally expressing Jaws or eNpHR3.0 in the ACC and implanting an optic fiber cannula over

SC_m to target its outputs for inactivation. Remarkably, inactivating the ACC-SC output pathway increased erroneous contra actions without affecting correct contra actions (Figure 1F). Thus, the ACC-SC pathway principally organizes behavioral performance in our task by suppressing erroneous contra actions (Figure 1E, Model 2).

Does the ACC also promote correct actions? We addressed this question by photostimulating ChR2-expressing inhibitory neurons in the ACC with blue light to directly inactivate it during the task. Regional ACC inactivation produced similar changes in behavior as observed with inactivation of SC_m and led to an overall decrease in contra actions (Figure 1G). Furthermore, this manipulation did not change the miss rate or movement start time, but reduced movement velocity on contra trials (Figure S3B). Thus, activity in ACC is also necessary for the expression of correct contra actions (Figure 1E, Model 1). Surprisingly, ACC inactivation did not increase incorrect actions as might be expected from the results of the ACC-SC pathway inactivation experiments (Figure 1F). Regional inactivation inhibits activity across a range of ACC projections in addition to the ACC-SC pathway, suggesting that top-down outputs to other target structures organize behavior by promoting contra actions. Hence, we further characterized the functional and anatomical architecture of the ACC to better understand the circuit mechanisms underlying goal-oriented action control in our task.

Functional and anatomical architecture of ACC circuits for bidirectional action control

Performance on our task crucially requires integration of inputs from the two halves of the visual field. We injected a rabies virus encoding a green or red fluorophore to identify the presynaptic sources of visual inputs to the caudal region of the ACC. As a comparison, we also injected a rabies virus encoding a different color fluorophore into the more rostral ACC region in which few outputs to SC_m were observed (Figure 2A). Although both compartments received inputs from medial higher visual cortex, corresponding to functionally-defined anteromedial and posteromedial areas (Wang and Burkhalter, 2007), the caudal ACC also received inputs from the primary visual cortex (Figure 2B-C). In addition, each compartment received prominent inputs from its counterpart in the contralateral hemisphere (Figure 2D), suggesting that visual information relayed from the visual cortex (VC) may be exchanged between the ACC hemispheres via callosal projections. We tested this possibility by using two-photon microscopy to image visually-evoked GCaMP6s responses of VC and callosal axons in the ACC (Figure 2E). While VC axons responded nearly exclusively to stimuli presented in the contralateral visual field (relative to the site of

recording), callosal axons responded preferentially to ipsilateral stimuli (Figures 2F-H; S5; S6). These observations, together with previous studies demonstrating that visual cortical areas have largely lateralized representations of stimuli and callosal connectivity limited to the midline of the visual field (Wang and Burkhalter, 2007), suggest that the caudal ACC is uniquely positioned to integrate extended visual inputs presented in either hemifield and bidirectionally organizes behavioral responses to them. We conceptualized a circuit diagram wherein the ACC organizes performance by biasing activity in SC_m either directly or indirectly to promote contra actions when they are instructed by the cue but to suppress them when ipsi cues are presented (Figure 2I).

How might ipsi cues suppress contra actions? One possibility is that ACC-SC neurons active on ipsi trials inhibit activity in SC_m, thus explaining why inactivating their outputs disinhibits erroneous contra movements (Figure 1E, F). We reasoned that since callosal axons convey sensory information for ipsi actions (Figure 2G, H; S6), photoactivating them could recruit these neurons and allow us to assess how they modulate activity in SC_m. We unilaterally expressed ChR2 in excitatory ACC neurons and placed an optic fiber cannula in the opposite ACC to target callosal inputs (Figure 3A, B). We made extracellular recordings of spontaneous activity with a 16-channel silicone probe in the SC_m ipsilateral to the site of the implanted fiber and activated callosal inputs with blue light. Laser activation of callosal ACC axons modulated the activity of 32.4% (24/75) of isolated single SC_m units (Wilcoxon signed-rank test, $p < 0.05$). Inspection of single-neuron responses showed a time-locked decrease in activity with laser activation (Figure 3C). Quantifying the effect of callosal photostimulation on the activity of all laser-modulated SC_m neurons showed that this manipulation led to a significant net decrease in activity (Figure 3D). We also directly activated ChR2-expressing ACC neurons to determine how non-specifically activating their outputs influences activity in SC_m (Figure S7A, B). This modulated the activity of a similar proportion of units in the ipsilateral SC_m as in the previous experiment (27.0%, 17/63 units from 3 mice), but individual neurons had both increased and decreased activity (Figure S7C, D). As a result, there was no net change in the activity of the population of laser-modulated neurons (Figure S7E). Hence, while selectively activating callosal ACC inputs largely inhibits SC_m, non-specific ACC activation both increases and decreases activity, suggesting that activity in SC_m is bidirectionally controlled by the ACC. Moreover, callosal inputs representing the ipsi cue may recruit ACC outputs that inhibit SC_m activity to suppress incorrect contra actions. At the same

time, other inputs to ACC may recruit output pathways that excite SC_m to promote correct contra actions.

Long-range cortical outputs are primarily glutamatergic and it is unclear how callosal activation suppresses activity in SC_m. We used anterograde transsynaptic viral tracing to test the possibility that ACC outputs target inhibitory neurons in SC_m (Zingg et al., 2017). We injected tdTomato reporter mice with an AAV1 virus expressing the Flpo recombinase in the ACC (Figure 3E) and performed immunohistochemistry against GABA in slices containing the SC_m (Figure 3F, G). Counting cells positive for tdTomato and GABA showed that ~30% of SC_m neurons that receive inputs from the ACC contained GABA and hence are likely to be inhibitory neurons (Figure 3H). Therefore, recruiting local inhibition in SC_m is a possible mechanism by which ACC-SC neurons inhibit activity in SC_m. to suppress erroneous contra actions in the presence of ipsi stimuli (Figure 2I).

ACC outputs to the superior colliculus predict ipsi actions

Next, we measured responses of ACC-SC neurons during the task to test a core prediction of our model, that ACC-SC neurons organize behavioral responses to ipsi stimuli. We used two-photon microscopy to image the activity of GCaMP6s-expressing layer 5 neurons back-labeled via injection of a retrograde tracer into SC_m (Figure 4A). Examination of single neuron responses on correct trials, with data aligned to stimulus onset, showed robust task-related activity in ACC-SC (Figure 4B) and unlabeled neuron populations (Figure S8A). While some individual neurons were active during correct contra or ipsi action trials, others responded non-specifically during either trial-type. We identified task-modulated neurons by comparing activity before and after stimulus onset. A majority of ACC-SC neurons imaged during the task (60.1%) showed task-modulated activity. Next, we computed a trial preference score for each task-modulated neuron and used a permutation test ($p < 0.05$) to find cells that were preferentially active on contra or ipsi trials (Figures 4C, D; S8). Overall, 65% of ACC-SC neurons with significant trial preference were active on correct contra and 35% on correct ipsi trials. Since we observed a similar pattern of activity between ACC-SC and unlabeled neurons, it is likely that additional ACC output pathways also contribute to action control in our task.

Next, we investigated whether task-responses of ACC-SC neurons represent sensory or movement information. We reasoned that since the same visual cue is presented on either correct or error trials, neurons representing the stimulus would respond similarly under both conditions.

Likewise, since animals make opposite movements on these trials, we would expect neurons that represent the movement direction to have different activity. We differentiated between responses on contra and ipsi trials by comparing the activity of ACC-SC neurons preferentially active on either trial-type. Examining single-neuron and population averaged responses showed that contra-preferring ACC-SC neurons responded similarly on correct and error trials (Figure S9A-C). In contrast, responses of ipsi-preferring ACC-SC neurons were differentially modulated (Figure S9D-F). We further examined this phenomenon by training linear decoders (Graf et al., 2011; Morcos and Harvey, 2016; Raposo et al., 2014) with single-trial responses of contra- or ipsi-preferring ACC-SC neurons to predict the location of the visual cue presented (cue decoder) or the action expressed by the animal (movement decoder; Figure 4E; see Methods). Decoders trained with the activity of either contra- or ipsi-preferring ACC-SC neurons performed better than chance at predicting the visual cue location or the movement direction (compared to shuffled data, $p < 0.01$). However, cue decoders trained with the activity of contra-preferring ACC-SC neurons were better at predicting the location of the visual cue, whereas movement decoders trained with the activity of ipsi-preferring neurons were better at predicting the movement direction (Figure 4F). Thus, while contra-preferring ACC-SC neurons contain more cue information, ipsi-preferring ACC-SC neurons contain more movement information. Together with the findings that inactivating ACC-SC projections increases errors on ipsi trials (Figure 1F), and that ipsi-informative projections inhibit SC_m (Figure 3D), these results suggest that ipsi-preferring ACC-SC neurons promote ipsi actions by suppressing incorrect contra actions (Figure 2I).

ACC outputs to the visual cortex promote correct contra actions

Although the ACC-SC pathway primarily promotes ipsi actions, imaging of non-SC projecting ACC neurons revealed robust responses on contra trials (Figure S8B). In addition, regional inactivation of the ACC decreased contra actions (Figure 1G), suggesting that the ACC also contributes to contra performance. The ACC sends dense outputs to the VC and modulates its activity (Leinweber et al., 2017; Zhang et al., 2016; Zhang et al., 2014). The VC in turn projects to and modulates activity in the SC (Zhao et al., 2014), suggesting that the ACC-VC pathway may drive contra actions by indirectly modulating activity in the SC_m (Figure 5A). We set up a linear model based on the anatomical, functional, and behavioral data obtained thus far to better understand how projections between ACC, VC, and SC_m interact to produce the observed behavioral performance (Figure S10A; see complete details in Methods). We were specifically

interested in formally testing our reasoning that the ACC-VC pathway indirectly excites the SC and promotes contra actions. We defined the activity of each SC_m hemisphere as a linear sum of four input pathways on contra and ipsi trials: 1) direct ACC-SC pathway that excites the SC on contra trials, 2) direct ACC-SC pathway that inhibits the SC on ipsi trials, 3) an ACC-VC pathway that indirectly excites the SC on contra trials (ACC-VC-SC), and 4) a pathway representing the baseline task-independent activity of the SC. Based on previous studies (Felsen and Mainen, 2012), we modeled behavioral performance as a function of the difference in activity between the two hemispheres of SC_m such that the side with higher activity leads to its preferred contra movement (Figure S10B). We represented three crucial optogenetic experiments (inactivation of ACC, SC, and ACC projections to the SC; Figure S10C) in the model and used the behavioral performance observed on them to derive estimates for the contribution of these four pathways to activity in SC_m during the task (Figure S10D, E). Next, we simulated the inactivation of ACC outputs to the VC in the model (Figure S10D); using these estimates led to the prediction that the ACC-VC-SC pathway promotes contra actions (Figure S10E). Hence, inactivating ACC outputs to the VC should decrease the selection of contra actions.

As a first test of this prediction, we determined the contribution of VC to task performance. Unilaterally inactivating the VC by delivering yellow light onto Jaws-expressing neurons decreased the expression of contra actions (Figure S11A). While this manipulation did not change the movement start time or velocity, there was an increase in the miss rate on contra stimulus trials (Figure S11B-D). This suggests that ACC may promote contra actions by modulating activity in VC. Since our model predicted that the ACC-VC and ACC-SC pathways control opposite actions in our task, we tested if there is anatomical segregation in the population of ACC neurons that project to these areas. We injected rabies viruses encoding either GFP or tdTomato in the VC and SC_m and quantified the number of back-labeled neurons in the ACC. Consistent with a previous study (Zhang et al., 2016), we found that non-overlapping sets of ACC neurons targeted these structures (Figure 5B, C). Next, we directly tested the model prediction that the ACC-VC pathway drives contra actions by expressing Jaws in the ACC and placing a chronic window over the VC to inactivate ACC output axons during the task (Figure 5D). Inactivating the ACC-VC pathway decreased correct contra actions (Figure 5E), as predicted by the model (Figure S10). Comparing the effect of inactivating the ACC-SC and ACC-VC pathways showed that ACC outputs to SC_m suppress, and outputs to VC promote, contra actions (Figure 5F). Together, our results show that

the ACC organizes behavioral performance using distinct population of projection neurons that exert bidirectional control over goal-oriented actions.

Discussion

Our experiments identify specific inputs to and outputs from PFC that together coordinate bidirectional control of sensory-guided actions (Figure 5A). We show that VC inputs bring information about the contralateral stimulus, whereas callosal inputs convey the presence of ipsilateral stimuli to the ACC (Figure 2A-H; Figures S5, S6). Using an SC_m-dependent action control task in head-fixed mice that also requires activity in the VC and the ACC (Figures 1C, G; S11), we show that these inputs enable the top-down modulatory role of ACC, as calcium imaging of task-responses from ACC neurons show that individual neurons are preferentially active on both contra and ipsi action trials (Figures 4C; S8B). The activity of ACC-SC neurons predicts ipsi movements (Figure 4F). Mimicking the presence of cues instructing ipsi actions through photostimulation of callosal inputs potentially recruits local inhibition to suppress activity in SC_m (Figure 3). Furthermore, disinhibiting SC_m by removing this inhibitory drive increases erroneous contra actions (Figure 1F). At the same time, inactivation of a parallel output pathway from the ACC to the VC inhibits correct contra actions (Figure 5E). Thus, the ACC-SC pathway inhibits incorrect actions, whereas the ACC-VC pathway promotes correct actions (Figure 5A).

Each hemisphere of SC_m coordinates movements to the contralateral hemifield and competition between the two sides of SC_m via mutual inhibition has been proposed as a potential mechanism underlying performance in two-choice action tasks (Felsen and Mainen, 2012). Our results suggest that such a competition first takes place within each hemisphere of SC_m and is arbitrated through distinct PFC output pathways that increase or decrease activity levels in the SC_m to promote or suppress specific movements. Due to the lateralized nature of stimulus representation in the visual system, the ACC likely constitutes one of very few extrinsic inputs to SC_m that represent the ipsilateral stimulus and hence can serve uniquely to suppress erroneous contra movements in the presence of such stimuli. In agreement, we found that although direct photostimulation of the ACC had a heterogeneous effect on the activity of SC_m, selective activation of callosal inputs, which represent ipsilateral stimuli (Figures 2G, H; S6), suppressed activity in SC_m (Figure 3A-D). Although the simplest interpretation of these results is that callosal activation recruits a subset of ACC-SC neurons that directly inhibit SC_m by recruiting local inhibition (Figure

3E-H), we cannot rule out the possibility that these inputs recruit ACC projections to an intermediary area(s) which then inhibits SC_m. Nonetheless, using projection-specific optogenetics during the task, we provide clear evidence that direct projections from ACC to SC_m exert inhibitory control over behavior by suppressing incorrect contra actions (Figure 1F).

While responses of ACC-SC neurons on ipsi trials are necessary for this inhibitory control, our experiments show that ACC-SC neurons are also active on contra trials (Figure 4C). However, ACC inputs to SC_m are not necessary for contra actions under our task conditions (Figure 4C). This suggests that the contribution of ACC inputs to contra performance may be redundant to inputs that the SC_m receives from other sources. Our decoding analysis suggests that these neurons predominantly carry stimulus information (Figure 4F). The sensory layer of the SC receives strong visual drive directly from the retina and the visual cortex (Hofbauer and Drager, 1985; Wang and Burkhalter, 2013), and can drive movements via feedforward projections to SC_m. Thus, inputs from the sensory SC and other sources may compensate for ACC outputs to SC_m on contra trials.

Although ACC inputs to SC_m organize performance by inhibiting incorrect contra actions, we found that the ACC uses an anatomically non-overlapping but functionally complementary population of projection neurons to promote actions through the visual cortex (Figure 5E). These results are consistent with a recent study showing that photoactivation of ACC outputs to the VC promotes turning in locomoting mice traversing a virtual corridor (Leinweber et al., 2017) and with studies in monkeys showing that stimulation of the visual cortex evokes saccadic eye movements (Tehovnik et al., 2003). While the exact mechanisms mediating motor responses through the visual cortex are unclear, ACC outputs to VC may promote contra actions by controlling VC outputs to multiple pathways that converge in SC_m (Hikosaka et al., 2000; Wallace et al., 1990; Zhao et al., 2014).

Similar to previous studies (Erlich et al., 2011; Li et al., 2015), we also found that non-discriminate, regional inactivation of an area in the frontal cortex decreased contra performance (Figure 1G), which at first sight would suggest that it only promotes such behavior. However, our results highlight the difficulty in ascribing functional roles to specific brain areas by using only regional inactivation. Such manipulations simultaneously change activity across multiple output pathways and thus obscure the effect of individual, potentially antagonistic, outputs. By dissecting the contribution of individual outputs, our results highlight a candidate long-range circuit motif for PFC circuits wherein anatomically non-overlapping but functionally complementary output

projections exert control over common downstream motor structures to promote and inhibit behavior in a context-dependent manner.

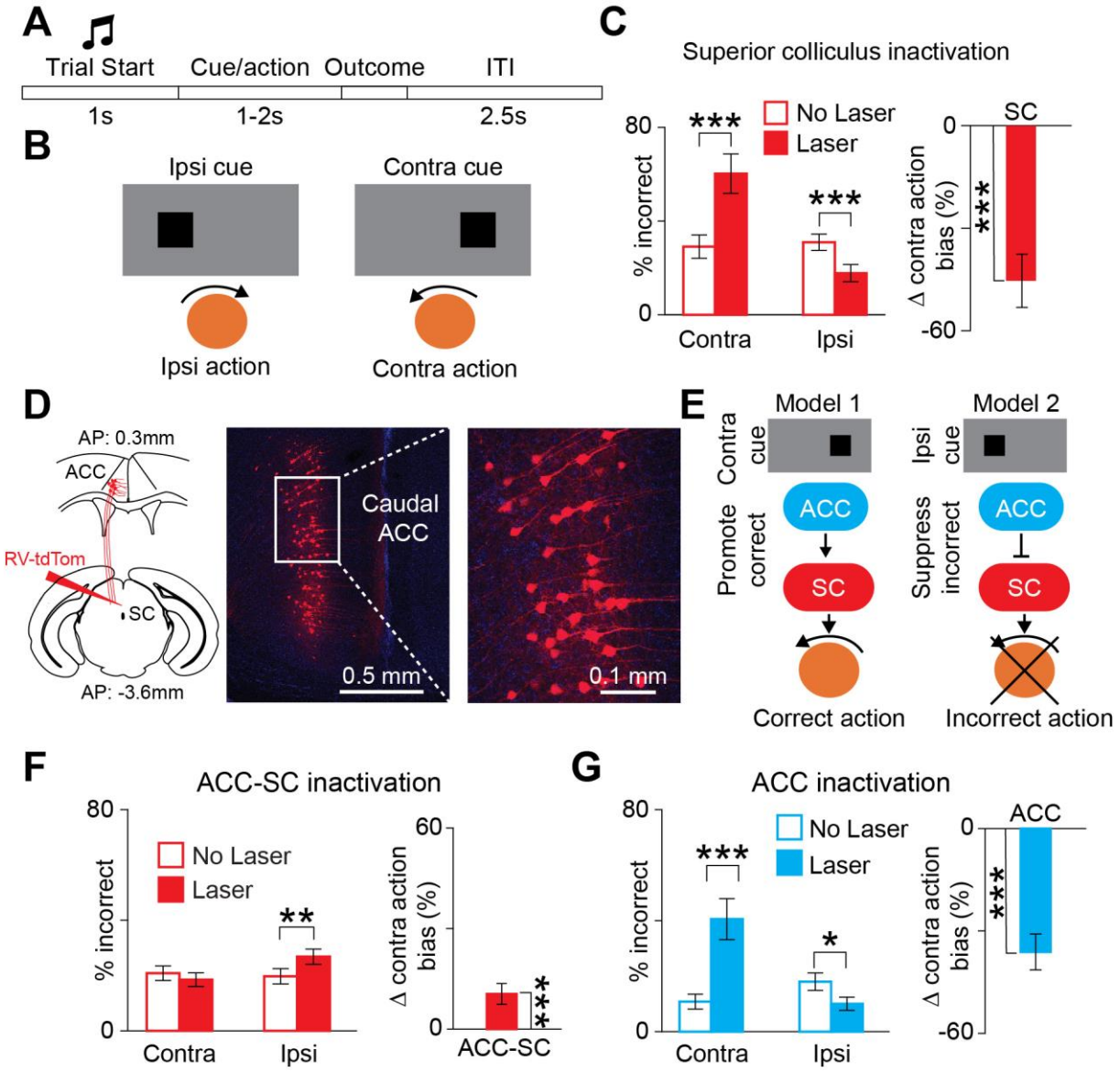

Figure 1. ACC facilitates behavior by suppressing incorrect and promoting correct actions. (**A**) Trial events during the task. (**B**) Schematic showing the behavioral setup. Mice move stimuli presented in either hemifield to the center by rotating a trackball. (**C**) Incorrect performance on contra and ipsi cue trials with (solid) and without (unfilled) SC inactivation (n = 10 sessions, 5 mice). Normalized laser-induced change in the expression of contra actions (proportion of trials with a contra movement out of all completed trials) is shown on right. (**D**) Rabies virus encoding tdTomato was injected in the SC (left). Back-labeled SC-projecting neurons in caudal ACC (right). (**E**) Two models for how ACC outputs to SC_m organize behavioral performance. (**F, G**) Similar to C, except for inactivation of ACC outputs to SC_m (n = 20 sessions, 7 mice) and regional photoinhibition of the ACC (n = 14 sessions, 5 mice). *p < 0.025, **p < 0.01, ***p < 0.005 (Wilcoxon signed rank or rank sum test). Significance evaluated at Bonferroni-adjusted p-value of 0.025. All error bars show standard error of the mean. *See also Figures S1-S4.*

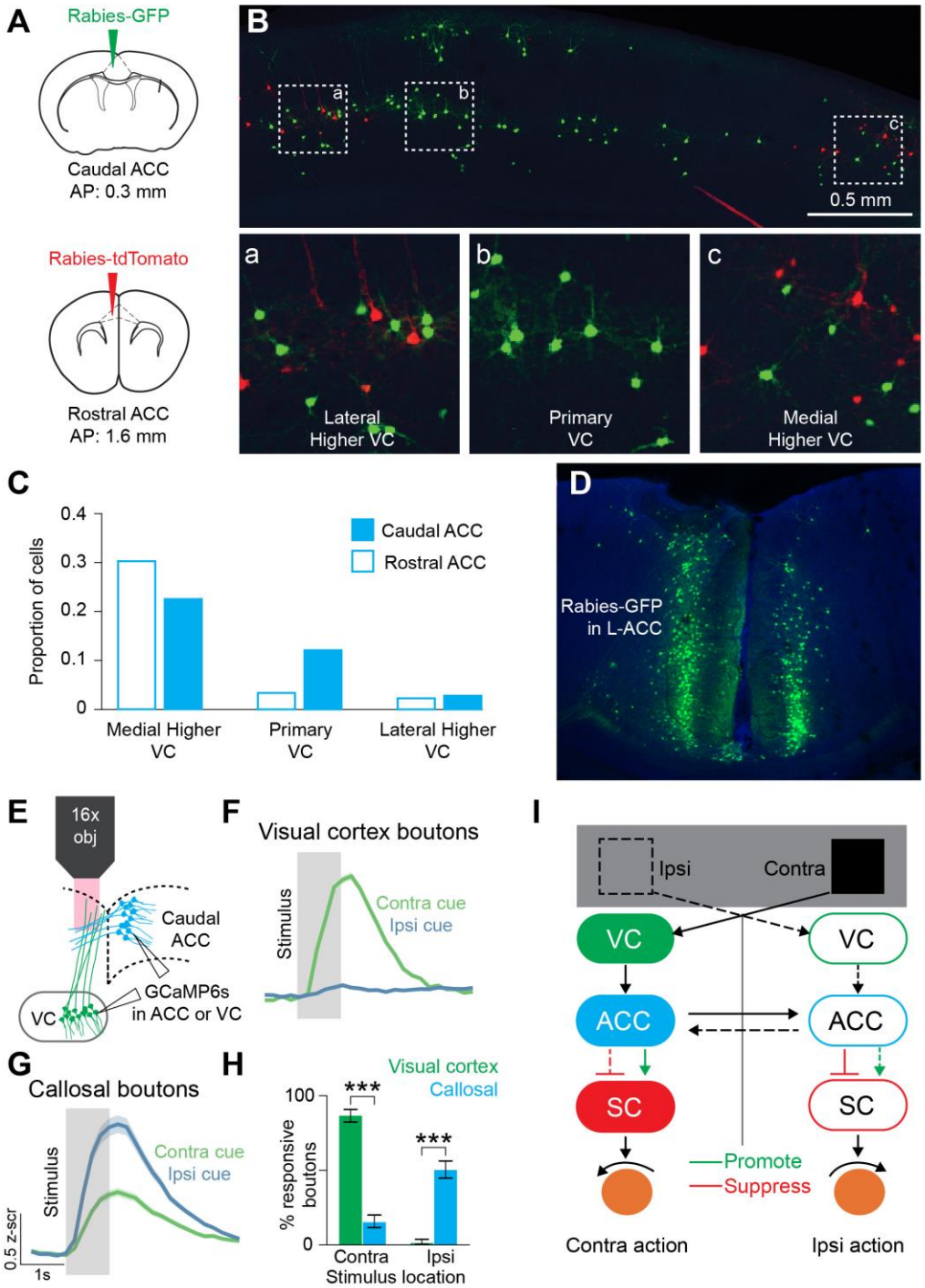

Figure 2. Anatomical and functional characterization of inputs to and outputs from the ACC. (**A**) Rabies viruses encoding GFP or tdTomato were injected into caudal or rostral ACC, respectively. (**B**) Back-labeled neurons in the visual cortex. Neurons in lateral higher VC, primary VC, or medial higher VC are denoted by dotted squares (a-c) on top and shown at higher magnification on the bottom. (**C**) Proportion of back-labeled neurons in various VC subdivisions projecting to caudal (solid) or rostral (unfilled) ACC (n = 3 mice). (**D**) Back-labeled callosal caudal ACC neurons. (**E**) Experimental setup for two-photon imaging of GCaMP6s-expressing visual cortex or callosal axons in the ACC while head-fixed mice passively viewed visual stimuli (black

square or grating, ~20º) presented in either hemifield. (**F, G**) Population-averaged responses of visually-driven VC (n = 268 boutons from 5 mice) and callosal (n = 309 boutons from 4 mice) boutons to stimuli presented in contra- and ipsilateral hemifield. Solid line is the mean response and shading shows the standard error of the mean. (**H**) Percent of visually-driven VC and callosal boutons with preferential responses to contra or ipsi stimuli. Errors bars are 95% binomial confidence intervals. (**I**) Circuit model for role of specific inputs to and outputs from ACC in promoting and suppressing actions. ***$p < 0.005$ (Fisher's exact test). *See also Figures S5-6.*

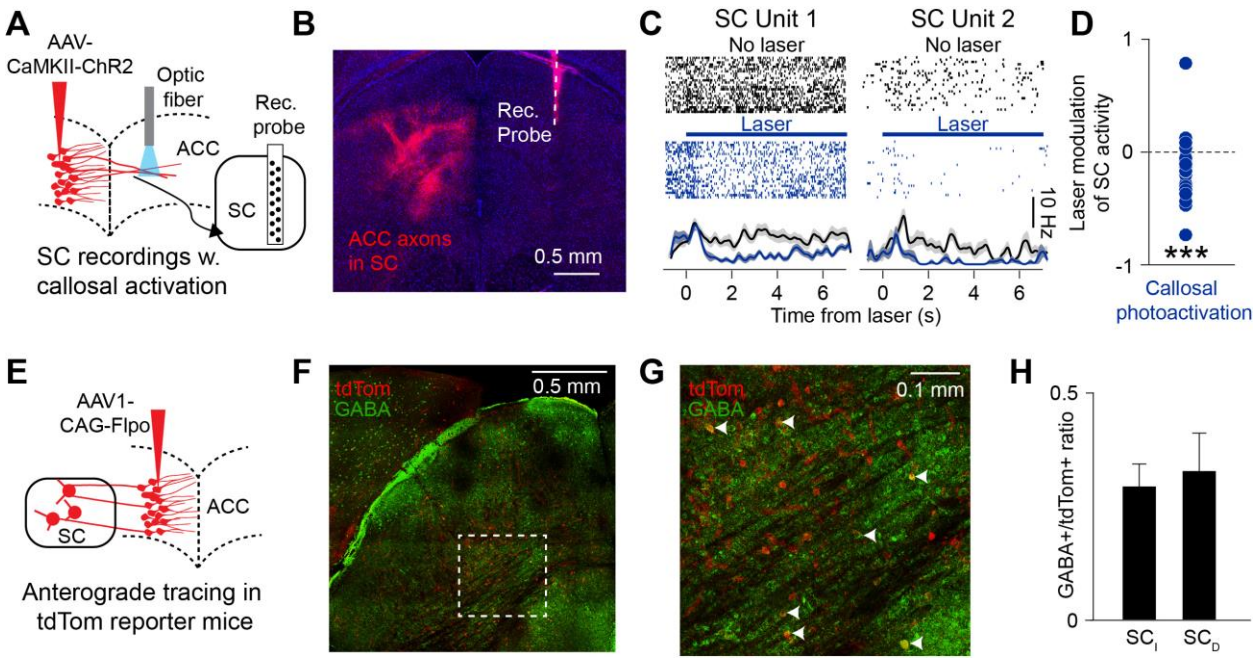

Figure 3. Callosal inputs to ACC suppress activity in SC_m. (**A**) AAV virus encoding CaMKII-ChR2-mCherry was injected unilaterally in the ACC and an optic fiber was implanted in the opposite hemisphere. Extracellular recording probe was inserted on the same side as the optic fiber in SC_m. (**B**) ChR2-mCherry expressing ACC axons in the SC_m and the recording probe track. (**C**) Spontaneous activity of two example SC units with and without photostimulation of callosal axons. (**D**) Laser-modulation indices of single SC_m units with photostimulation of callosal axons. (**E**) Anterograde tracing of ACC outputs to the SC using AAV1 viruses. (**F**) Anterogradely labeled tdTomato-expressing (red) and GABA-containing neurons (green). (**G**) Higher magnification image of the area bounded by dotted white square in F. Arrowheads mark neurons double-labeled with tdTomato and GABA. (**H**) Proportion of tdTomato-expressing SC neurons co-labeled with GABA in intermediate (SC_i) and deep layers (SC_d). Error bars are standard error of the mean. ***$p < 0.005$ (Wilcoxon signed-rank test). *See also Figure S7.*

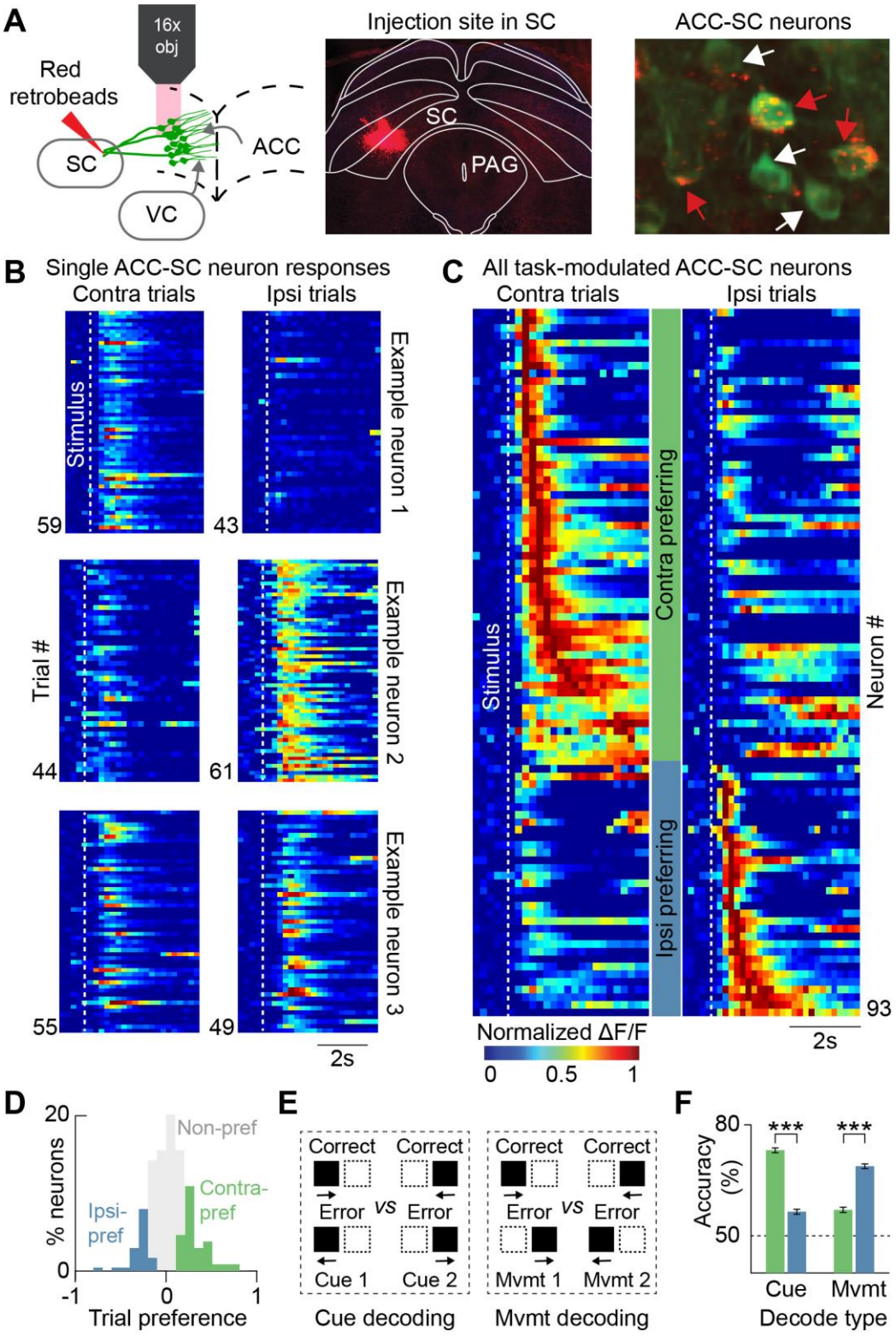

Figure 4. Task activity of ACC-SC neurons predicts ipsi actions. (**A**) GCaMP6s-imaging of layer 5 during the task. ACC-SC neurons were identified by injecting red retrobeads in SC_m. Recordings were made from 1572 neurons in five expert mice (12 behavioral sessions, 2-3 sessions

per animal), of which 416 were ACC-SC neurons. (**B**) Single-trial responses of three representative ACC-SC neurons on correct contra- and ipsi trials. (**C**) Session-averaged task-responses of individual ACC-SC neurons (rows). Responses are grouped by trial preference and sorted within each group by the time of peak response. Color bar applies to all color plots. (**D**) Distribution of trial preference scores for task-modulated ACC-SC neurons. (**E**) Combination of correct and error trials used for decoding cue or movement information. (**F**) Predictive accuracy of cue or movement decoders trained with the activity of contra- or ipsi-preferring ACC-SC neurons. Dotted line shows chance decoder performance. ***$p < 10^{-5}$ (Wilcoxon rank-sum test). Significance evaluated at Bonferroni-adjusted p-value of 10^{-5}. Error bars are 95% bootstrap confidence intervals. *See also Figures S8-9.*

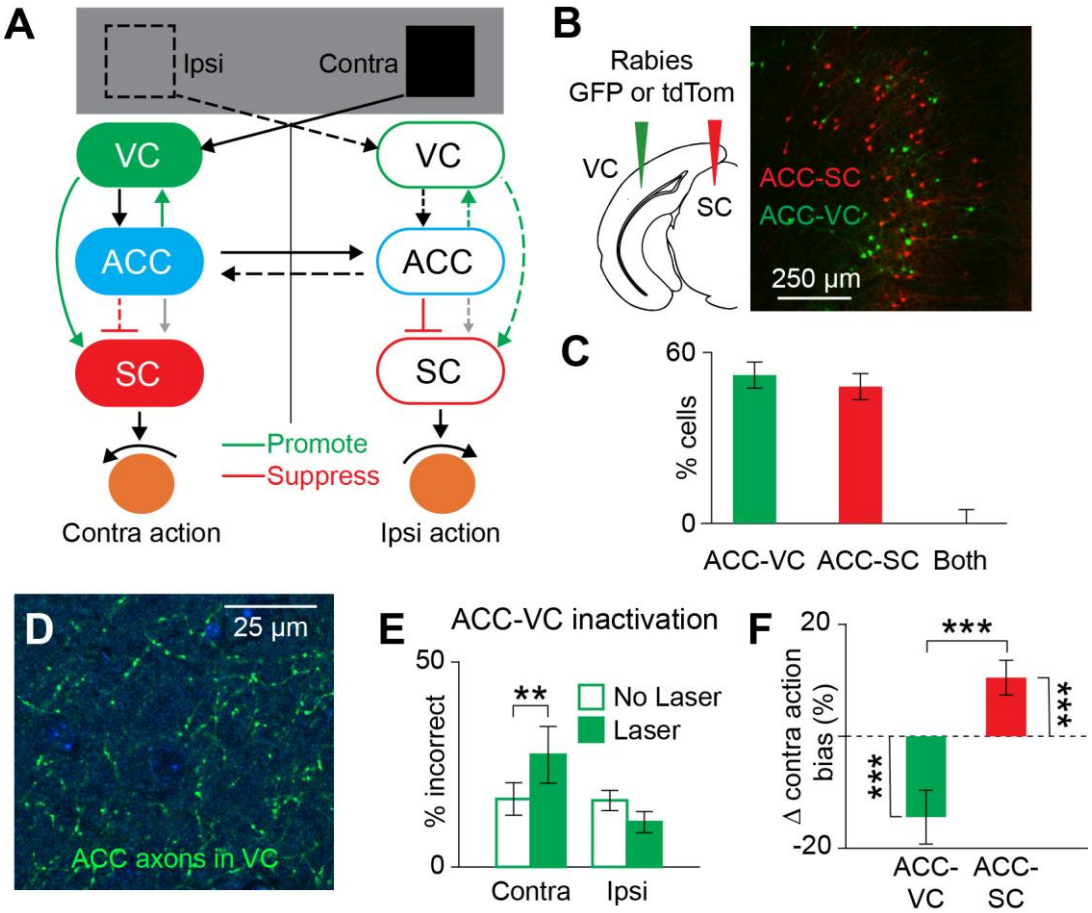

Figure 5. ACC outputs to the VC promote correct actions. (**A**) Circuit model for bidirectional action control by distinct ACC outputs. (**B**) Dual-color retrograde tracing from VC and SC_m. Back-labeled ACC neurons projecting to SC_m (red) or VC (green). (**C**) Proportion of back-labeled neurons projecting to either or both areas (n = 3 animals). (**D**) ACC was injected with an AAV virus expressing CaMKII-Jaws-GFP and its outputs to the VC were inactivated with yellow light through a chronic window. (**E**) Mean incorrect performance with (filled) and without (unfilled) photoinhibition of ACC outputs to the VC (n = 12 sessions, 4 mice). (**F**) Comparison of normalized laser-induced change in contra actions with inactivation of ACC outputs to VC (green) or SC_m (red). **$p < 0.01$, ***$p < 0.005$ (Wilcoxon signed rank or rank sum test). Significance evaluated at Bonferroni-adjusted p-value of 0.025. Error bars in C are 95% binomial confidence intervals and in E, F are standard error of the mean. *See also Figures S10-11*

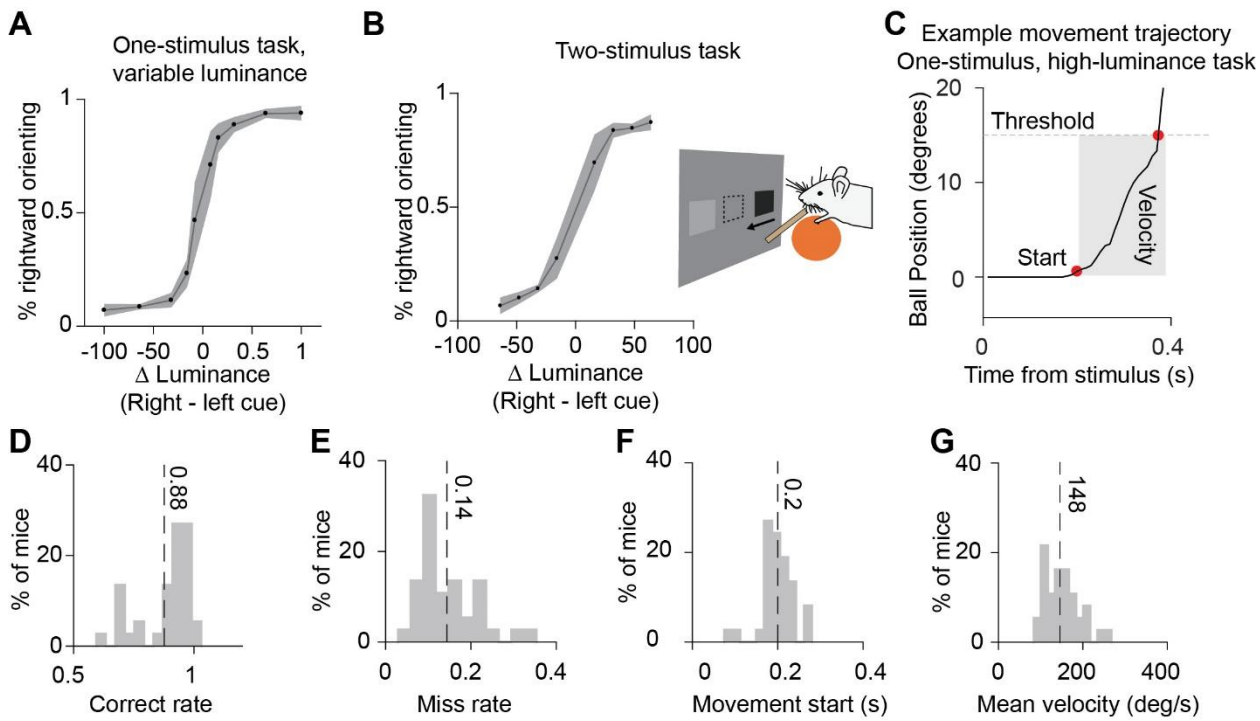

Figure S1. Performance on the behavioral task, Related to Figure 1. (**A**) Psychometric curve showing performance on the task with stimuli of varying luminance (n = 3-6 mice for each luminance). (**B**) Psychometric performance on two-stimulus variant of the task (n = 3-5 mice for each luminance pair). (**C**) Example movement trajectory trace. Kinematic analysis was used to detect the movement start time. Average instantaneous movement velocity was calculated between movement start time and the time at which the ball position reached the threshold (dotted line). (**D-G**) Probability distributions for correct rate, miss rate, movement start time, and mean instantaneous movement velocity across a cohort of mice (n = 37 mice). Mean values are shown with dotted vertical lines. Shading in A, B is standard error of the mean.

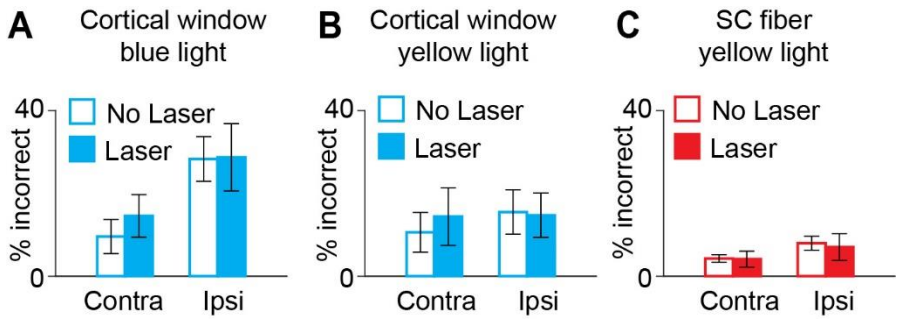

Figure S2. Light delivery in the absence of opsins does not affect behavioral performance, Related to Figure 1. (**A, B**) Mice were implanted with a chronic window over the ACC. No opsin-expressing viruses were injected on the side that was targeted with blue (n = 6 sessions from 2 mice) or yellow light (n = 9 sessions from 3 mice, 20mW). Mean error rate on contra and ipsi trials with and without laser is shown. (**C**) Same as A, B, except yellow light was delivered to SC_m through an implanted fiber optic cannula (n = 6 sessions from 2 mice). Error bars are standard error of the mean.

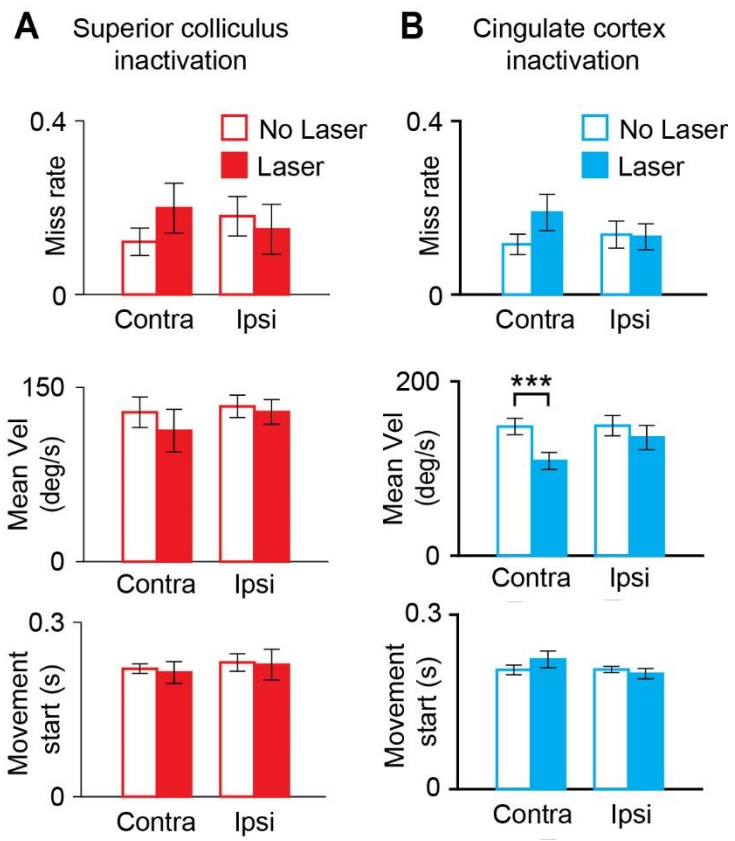

Figure S3. Effect of photoinhibition of SC_m and ACC on the miss rate and movement metrics, Related to Figure 1. (A) Mean miss rate, movement velocity, and movement start time on contra and ipsi trials with (solid) and without (unfilled) inactivation (n = 11 sessions, 5 mice). (**B**) Similar to that in A, except for regional inactivation of the ACC (n = 14 sessions, 5 mice). ***$p < 0.005$, Wilcoxon signed-rank test. Significance evaluated at Bonferroni-adjusted p-value of 0.025. Error bars are standard error of the mean.

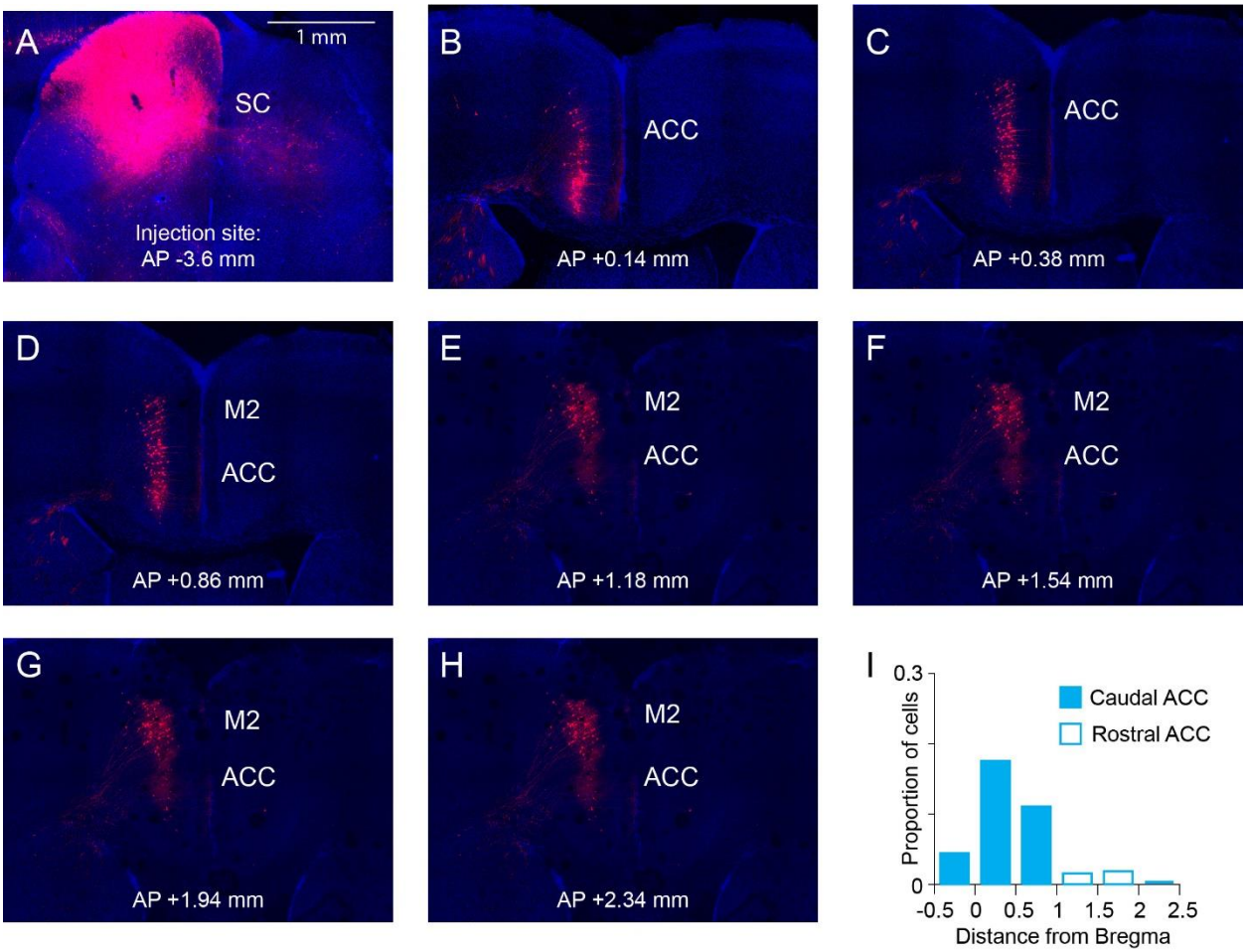

Figure S4. Motor and prefrontal cortex outputs to SC_m, Related to Figure 1. (**A**) Rabies virus expressing tdTomato (red) was injected in SC_m. (**B-H**) Back-labeled, tdTomato-expressing projection neurons found in secondary motor cortex (M2) and the ACC. Note that only cells ipsilateral to the site of injection are labeled. (**I**) Proportion of back-labeled SC-projecting neurons located along the caudo-rostral axis of the ACC (n = 2 animals).

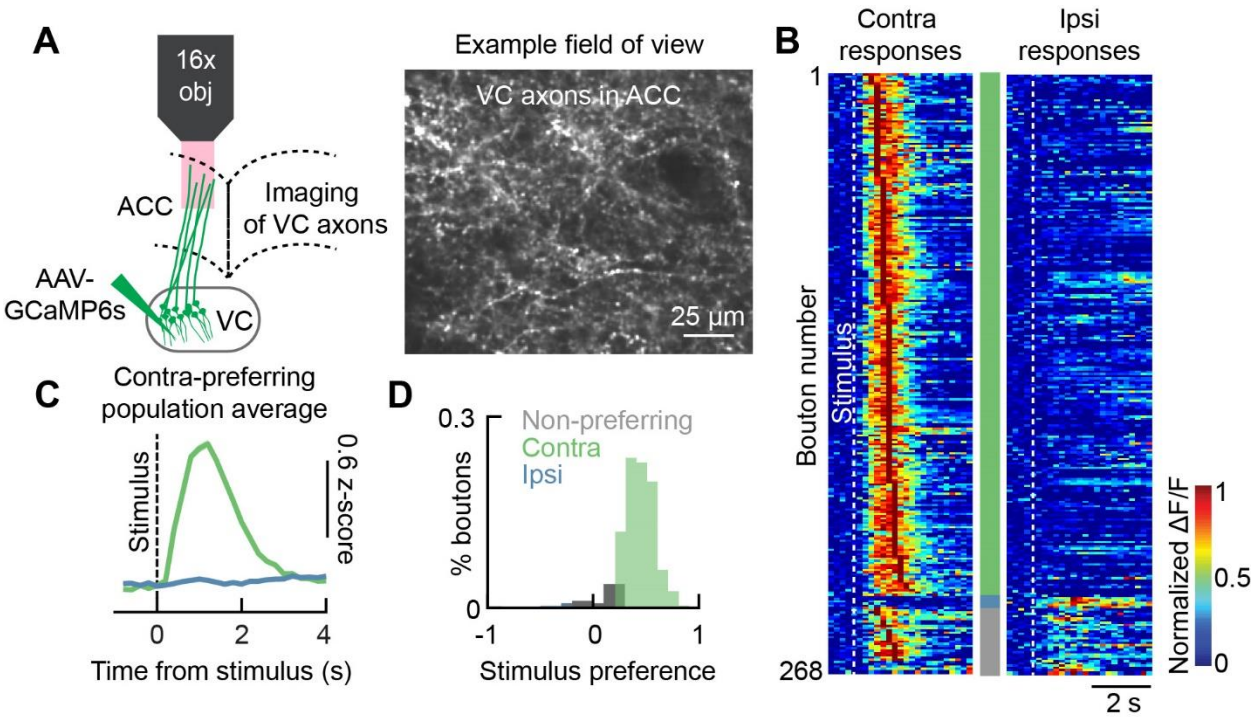

Figure S5. Visually-evoked responses of VC inputs to the ACC, Related to Figure 2. (**A**) Two-photon imaging of GCaMP6s-expressing VC axons in the ACC. (**B**) Session-averaged responses of individual visually-responsive boutons to stimuli presented in hemifield contra- or ipsilateral to the recording site (black square, ~20º size, 1s). Responses are grouped by their stimulus preference (contralateral, green; ipsilateral, blue, non-preferring, gray) and sorted within each group by their peak response time. (**C**) Population-averaged response of contra-preferring boutons to contralateral (green) and ipsilateral (blue) stimuli. Solid line is the mean response and shading shows the standard error of the mean. (**D**) AUROC analysis was used to calculate a stimulus preference score for each visually-responsive bouton. This score ranges from -1 (ipsi selective) to 1 (contra selective). Distribution of scores for 268 visually-responsive VC boutons in ACC from 4 mice is shown.

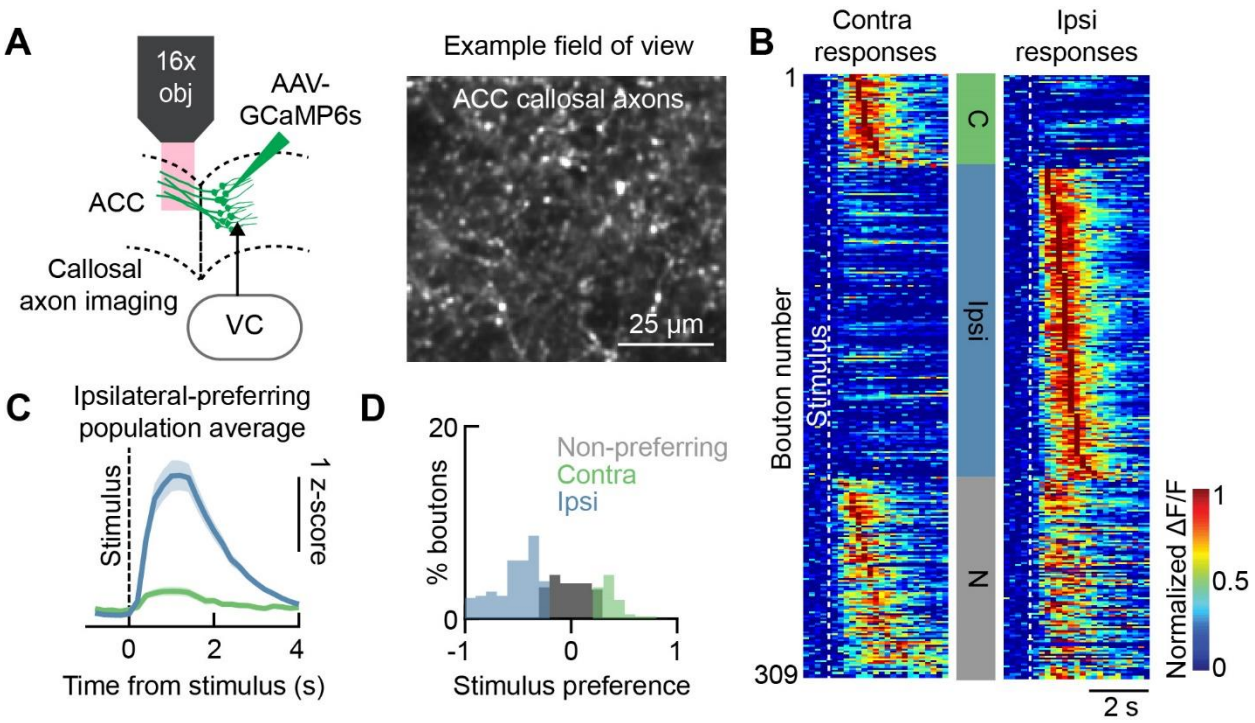

Figure S6. Visually-evoked responses of ACC callosal axons, Related to Figure 2. (**A**) Left, ACC was injected with an AAV virus expressing GCaMP6s and labeled axons were imaged through a chronic window over the opposite ACC. Right, Example field of view of GCaMP6s-expressing axons and boutons imaged in vivo. (**B**) Color map of session-averaged responses of individual visually-responsive boutons to stimuli presented contralateral or ipsilateral to the recording site (1s duration, 20º size, sinusoidal drifting grating). Responses are grouped by their stimulus preference (C, contra; N; non- preferring) and sorted within each group by their peak response time. (**C**) Population-averaged response of ipsilateral-preferring boutons to contralateral (green) and ipsilateral (blue) stimuli. Solid line is the mean response and shading shows the standard error of the mean (**D**) Histogram showing the distribution of stimulus preference scores for all visually-responsive callosal boutons (n = 309 boutons from 5 mice).

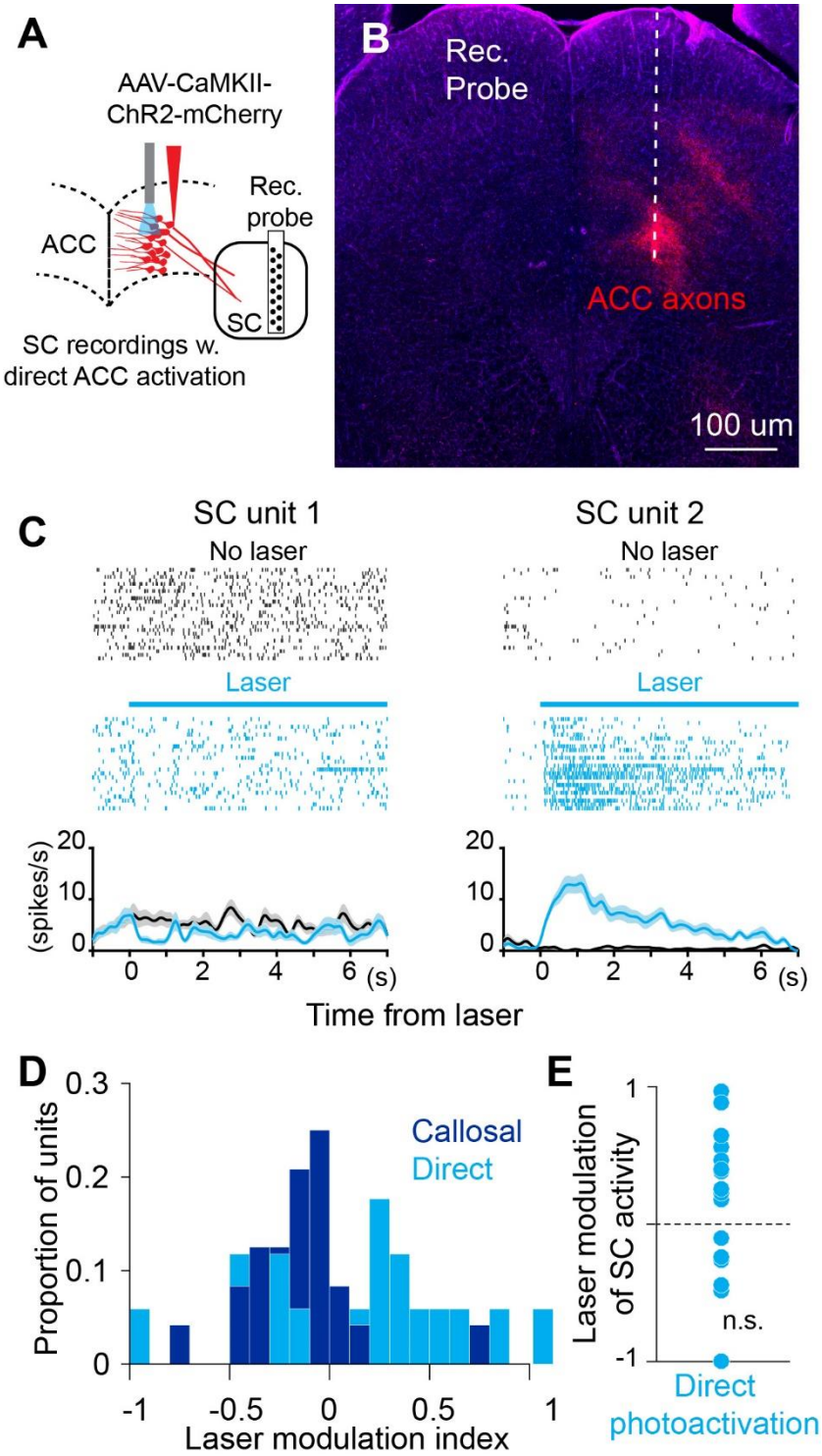

Figure S7. Effect of direct optogenetic activation of ACC neurons on single-unit activity in the SC_m, Related to Figure 3. (**A**) An AAV virus encoding CaMKII-ChR2-mCherry was injected in the ACC and an optic fiber was implanted on the same side. Extracellular recording probes were inserted in the SC ipsilateral to the fiber. (**B**) Histological section showing ChR2-expressing ACC axons in SC_m. Track made by the recording probe is also shown. (**C**) Activity of two example

single-units recorded in the SC with (blue) and without (black) optogenetic activation of the ACC. (**D**) Histogram depicting laser-modulation indices for single SC units with photoactivation of callosal inputs and of cell bodies in the ACC. Only cells significantly modulated by laser activation are included in this analysis. (**E**) Laser-modulation indices of single SC_m units with direct photostimulation of cell bodies in the ACC. Significance tested using Wilcoxon signed-rank test (n.s. represents $p > 0.05$).

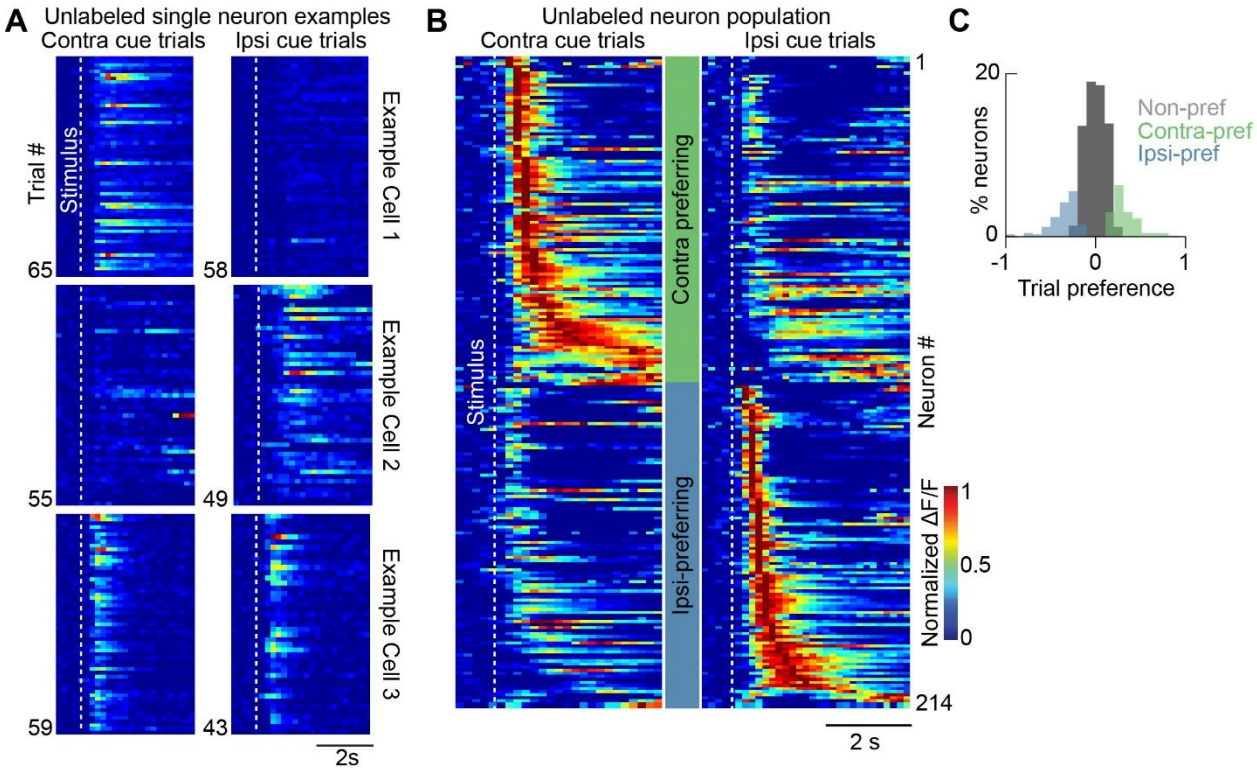

Figure S8. Calcium responses of non-SC$_m$ projecting ACC neurons during the task, Related to Figure 4. (**A**) Task- responses of three unlabeled ACC neurons on correct contra and ipsi trials. (**B**) Color map showing session-averaged responses of individual task-modulated non-SC projecting neurons (rows) on the indicated correct trials. Responses are grouped by trial preference and sorted within each group by the time of peak response. Stimulus onset is denoted by the white dotted line. Color bar also applies to B. (**C**) Distribution of trial preference scores for task-modulated non-SC projecting neurons.

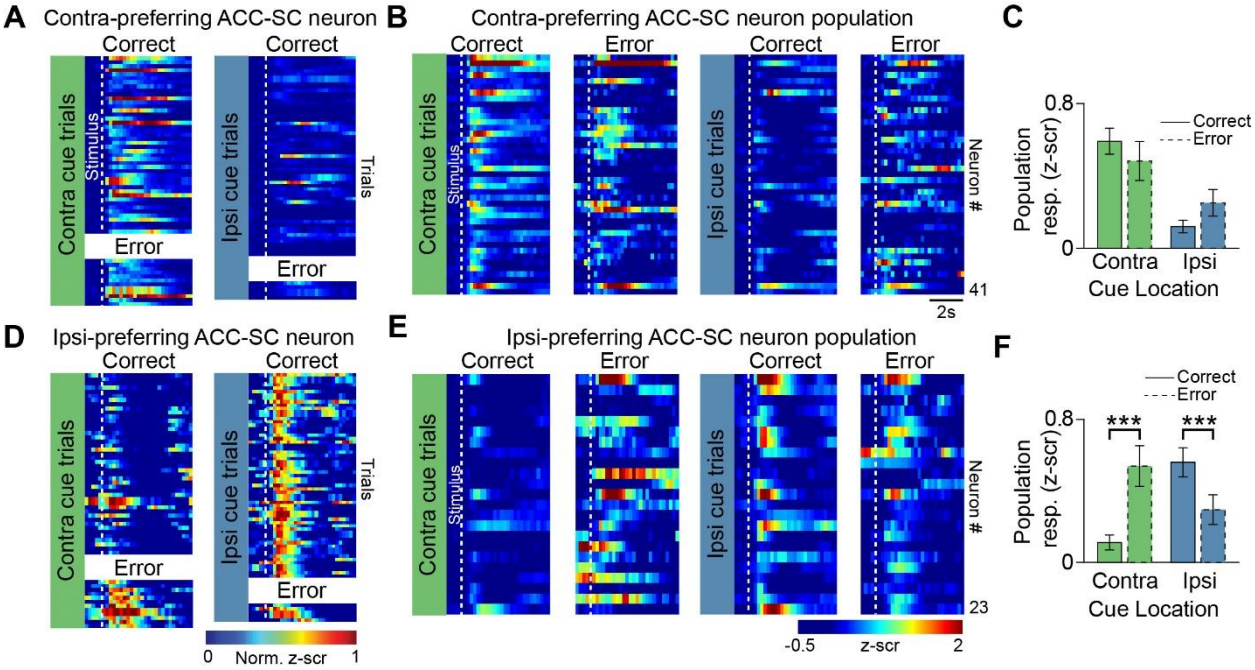

Figure S9. Error modulation of ACC-SC task-responses, Related to Figure 4. (**A**) Single-trial responses (rows) of an example contra-preferring ACC-SC neuron on correct and error trials. (**B**) Session-averaged responses of single contra-preferring ACC-SC neurons (rows) on correct and error trials. Neurons are sorted by their trial preference score. Only sessions with at least 5 trials in each condition are included. (**C**) Population activity (averaged over 1s after stimulus onset) of contra-preferring ACC-SC neurons on correct (solid) and error (dotted) contra (green) or ipsi (blue) cue trials. (**D-F**) Same as A-C, except for ipsi-preferring neurons. Scale bars shown in D and E also applies to A and B, respectively. ***$p < 0.005$; Wilcoxon signed-rank test. Significance evaluated at Bonferroni-adjusted p-value of 0.025. Error bars are standard error of the mean.

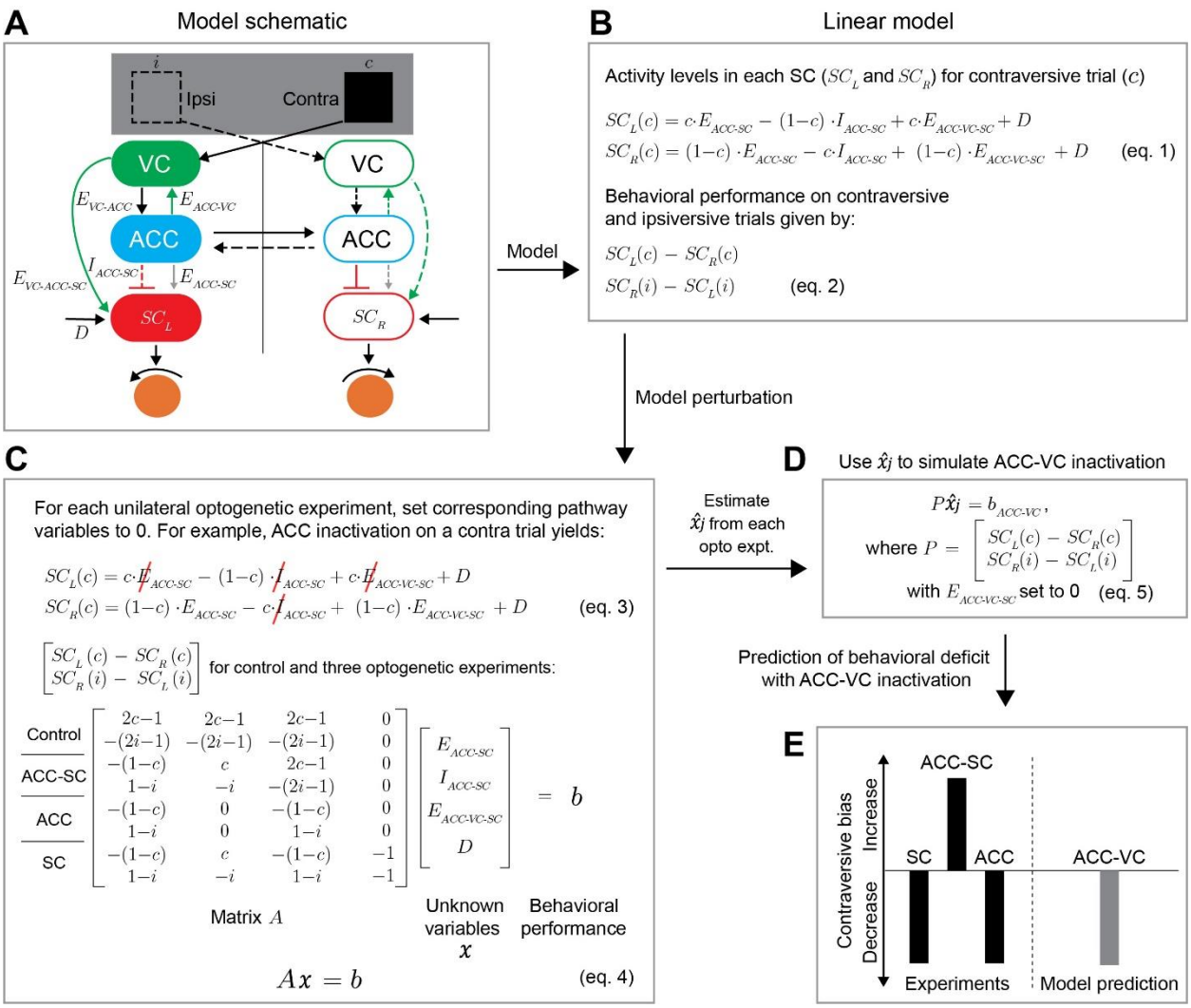

Figure S10. Linear activity model for predicting the effect of inactivation of ACC outputs to the VC, Related to Figure 5. (**A**) An anatomically-inspired linear activity model was used to predict the contribution of ACC-VC to action selection in the task (see Methods for complete details). The schematic assumes that the left side of the brain was inactivated and accordingly designates stimuli as contralateral or ipsilateral. Activity in SC_L (i.e., left SCm) and SC_R was expressed as the linear sum of activity from four excitatory input pathways: 1) direct ACC-SC pathway that excites the SC on contra trials ($E_{ACC\text{-}SC}$); 2) direct ACC-SC pathway that inhibits the SC on ipsi trials ($I_{ACC\text{-}SC}$); 3) ACC-VC pathway that excites the SC on contra trials ($E_{ACC\text{-}VC\text{-}SC}$), and 4) a pathway representing the baseline, task-independent activity of the SC (D). (**B**) Equations relating contributions of these pathways to activity in the two SCm hemispheres (SC_L, SC_R). We parameterized the contribution of the ACC-SC and ACC-VC-SC pathways by variables c and i representing the observed proportion of ACC-SC neurons preferentially active on contra and ipsi trials, respectively ($c = 0.65$ and $i = 0.35$; see Methods). Each trial type is described by two equations that express activity in SC_L and SC_R on that trial; eq. 1 shows a pair of example equations for a contra trial. We assume that contra (or ipsi) movements result when $SC_L - SC_R > 0$ (or $SC_L - SC_R < 0$) for a given trial (eq. 2). (**C**) We derived a qualitative estimate (see below) for the contribution of each of the four inputs to activity in SCm by using the average behavioral

performance from control conditions and three crucial inactivation experiments (of the ACC, SC or ACC-SC). Optogenetic inactivation is represented in the model by setting the contribution of the corresponding pathway(s) to 0. Eq. 3 illustrates the representation of unilateral inactivation of the left ACC on a contra trial. Three of the four input pathways are dependent on the ACC and are set to 0 (red strikethroughs) for the SC_L equation. Note that the inhibitory $I_{ACC\text{-}SC}$ pathway in the right ACC is zeroed because it relies on callosal inputs from left ACC, which is inactivated in this example. Eq. 4 shows these equations derived in a similar way for control and optogenetic inactivation of the ACC, SC, and ACC outputs to the SC, and expressed in matrix form, for contra trials. Each pair of rows corresponds to a specific experiment, wherein the first row is SC_L - SC_R (as described for eq. 2) for contra and the second row for ipsi trials (Matrix A). The unknown variables are in vector x, and the observed behavioral performance for contralateral and ipsilateral stimulus trials for each experiment is given by vector b. Generically, this relationship is expressed as $Ax = b$. Determining the contribution of each pathway to the difference in activity between the two SC_m hemispheres, and hence the selection of contra or ipsi actions, requires solving for the unknown variables in vector x. We derived an estimate for this vector, termed $\hat{x}_j$, using a common linear algebra technique (least-squares approximation) from each of the three optogenetic experiments (denoted by the subscript j, see Methods). Note that $\hat{x}_j$ contains an estimate for the ACC-VC-SC pathway ($E_{ACC\text{-}VC\text{-}SC}$), but the behavioral results from its optogenetic inactivation were not included in the derivation of $\hat{x}_j$. (**D**) We simulated inactivation of the ACC-VC pathway on the left side by setting $E_{ACC\text{-}VC\text{-}SC}$ to 0 and derived an equation for the difference in activity between the two SC_m hemispheres ($SC_L - SC_R$) for contralateral and ipsilateral trials (eq. 5), similar to that done for deriving matrix A in eq. 3. Multiplying this matrix P by $\hat{x}_j$ gave three predictions of behavioral results expected from inactivation of ACC-VC pathway, one from each of the three optogenetic experiments considered in the model. (**E**) Schematic summary of behavioral results observed with inactivation of the SC, ACC, and ACC-SC pathway. The model predicts that inactivation of the ACC-VC pathway decreases the selection of contra actions.

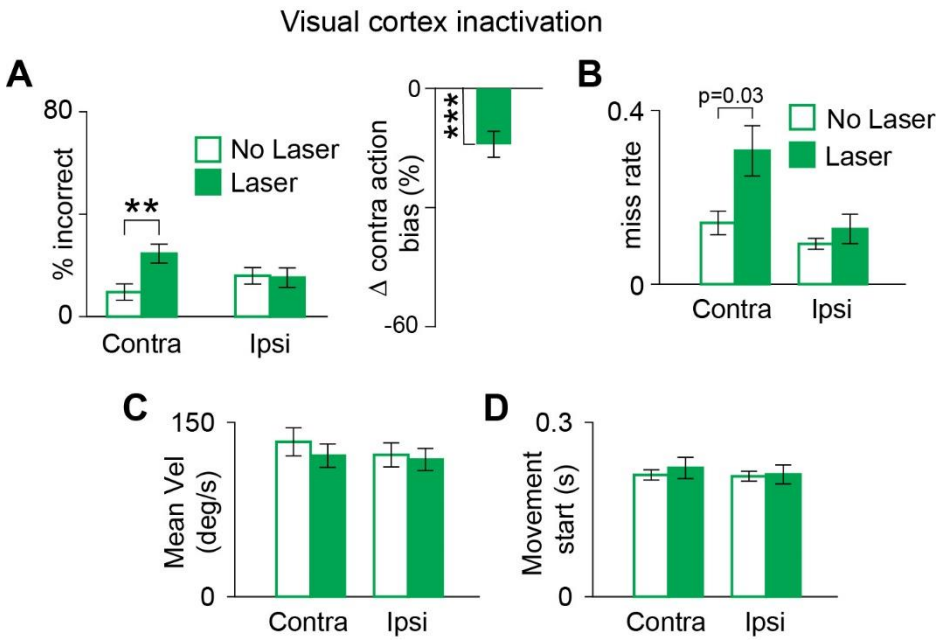

Figure S11. Visual cortex contributes to selection of contra actions, Related to Figure 5. (**A-D**) Mean incorrect performance, miss rate, movement velocity, and movement start time on contra and ipsi trials with (solid) and without (unfilled) VC inactivation (n = 11 sessions, 4 mice). **p < 0.01, (Wilcoxon signed-rank test). Significance evaluated at Bonferroni-adjusted p-value of 0.025. Error bars are standard error of the mean.

References

Armstrong, K.M., Chang, M.H., and Moore, T. (2009). Selection and maintenance of spatial information by frontal eye field neurons. J Neurosci *29*, 15621-15629.

Blanchard, D.C., Griebel, G., and Blanchard, R.J. (2001). Mouse defensive behaviors: pharmacological and behavioral assays for anxiety and panic. Neurosci Biobehav Rev *25*, 205-218.

Britten, K.H., Shadlen, M.N., Newsome, W.T., and Movshon, J.A. (1992). The analysis of visual motion: a comparison of neuronal and psychophysical performance. J Neurosci *12*, 4745-4765.

Bukalo, O., Pinard, C.R., Silverstein, S., Brehm, C., Hartley, N.D., Whittle, N., Colacicco, G., Busch, E., Patel, S., Singewald, N., *et al.* (2015). Prefrontal inputs to the amygdala instruct fear extinction memory formation. Sci Adv *1*.

Burgess, C.P., Lak, A., Steinmetz, N.A., Zatka-Haas, P., Bai Reddy, C., Jacobs, E.A.K., Linden, J.F., Paton, J.J., Ranson, A., Schroder, S., *et al.* (2017). High-Yield Methods for Accurate Two-Alternative Visual Psychophysics in Head-Fixed Mice. Cell Rep *20*, 2513-2524.

Chang, C.-C.L., C.-J (2011). LIBSVM: A library for support vector machines. ACM Trans Intell Syst Technol *2*, 1-27.

Chen, T.W., Wardill, T.J., Sun, Y., Pulver, S.R., Renninger, S.L., Baohan, A., Schreiter, E.R., Kerr, R.A., Orger, M.B., Jayaraman, V., *et al.* (2013). Ultrasensitive fluorescent proteins for imaging neuronal activity. Nature *499*, 295-300.

Choi, V.W., Asokan, A., Haberman, R.A., McCown, T.J., and Samulski, R.J. (2006). Production of recombinant adeno-associated viral vectors and use for in vitro and in vivo administration. Curr Protoc Neurosci *Chapter 4*, Unit 4 17.

Chung, J.E., Magland, J.F., Barnett, A.H., Tolosa, V.M., Tooker, A.C., Lee, K.Y., Shah, K.G., Felix, S.H., Frank, L.M., and Greengard, L.F. (2017). A Fully Automated Approach to Spike Sorting. Neuron *95*, 1381-1394 e1386.

Chuong, A.S., Miri, M.L., Busskamp, V., Matthews, G.A., Acker, L.C., Sorensen, A.T., Young, A., Klapoetke, N.C., Henninger, M.A., Kodandaramaiah, S.B., *et al.* (2014). Noninvasive optical inhibition with a red-shifted microbial rhodopsin. Nat Neurosci *17*, 1123-1129.

Cisek, P., and Kalaska, J.F. (2010). Neural mechanisms for interacting with a world full of action choices. Annu Rev Neurosci *33*, 269-298.

Cohen, J.D., McClure, S.M., and Yu, A.J. (2007). Should I stay or should I go? How the human brain manages the trade-off between exploitation and exploration. Philos Trans R Soc Lond B Biol Sci *362*, 933-942.

Dean, P., Mitchell, I.J., and Redgrave, P. (1988). Contralateral head movements produced by microinjection of glutamate into superior colliculus of rats: evidence for mediation by multiple output pathways. Neuroscience *24*, 491-500.

Erlich, J.C., Bialek, M., and Brody, C.D. (2011). A cortical substrate for memory-guided orienting in the rat. Neuron *72*, 330-343.

Fadok, J.P., Krabbe, S., Markovic, M., Courtin, J., Xu, C., Massi, L., Botta, P., Bylund, K., Muller, C., Kovacevic, A., *et al.* (2017). A competitive inhibitory circuit for selection of active and passive fear responses. Nature *542*, 96-100.

Felsen, G., and Mainen, Z.F. (2008). Neural substrates of sensory-guided locomotor decisions in the rat superior colliculus. Neuron *60*, 137-148.

Felsen, G., and Mainen, Z.F. (2012). Midbrain contributions to sensorimotor decision making. J Neurophysiol *108*, 135-147.

Ferenczi, E.A., Zalocusky, K.A., Liston, C., Grosenick, L., Warden, M.R., Amatya, D., Katovich, K., Mehta, H., Patenaude, B., Ramakrishnan, C., *et al.* (2016). Prefrontal cortical regulation of brainwide circuit dynamics and reward-related behavior. Science *351*, aac9698.

Frank, M.J., Doll, B.B., Oas-Terpstra, J., and Moreno, F. (2009). Prefrontal and striatal dopaminergic genes predict individual differences in exploration and exploitation. Nat Neurosci *12*, 1062-1068.

Franklin, K.B.J.P., G. (2013). Paxinos and Franklin's The mouse brain in stereotaxic coordinates (Boston, MA: Elsevier/Academic Press).

Goard, M.J., Pho, G.N., Woodson, J., and Sur, M. (2016). Distinct roles of visual, parietal, and frontal motor cortices in memory-guided sensorimotor decisions. Elife *5*.

Graf, A.B., Kohn, A., Jazayeri, M., and Movshon, J.A. (2011). Decoding the activity of neuronal populations in macaque primary visual cortex. Nat Neurosci *14*, 239-245.

Gregoriou, G.G., Gotts, S.J., and Desimone, R. (2012). Cell-type-specific synchronization of neural activity in FEF with V4 during attention. Neuron *73*, 581-594.

Grunfeld, I.S., and Likhtik, E. (2018). Mixed selectivity encoding and action selection in the prefrontal cortex during threat assessment. Curr Opin Neurobiol *49*, 108-115.

Hardung, S., Epple, R., Jackel, Z., Eriksson, D., Uran, C., Senn, V., Gibor, L., Yizhar, O., and Diester, I. (2017). A Functional Gradient in the Rodent Prefrontal Cortex Supports Behavioral Inhibition. Curr Biol *27*, 549-555.

Harvey, C.D., Coen, P., and Tank, D.W. (2012). Choice-specific sequences in parietal cortex during a virtual-navigation decision task. Nature *484*, 62-68.

Hikosaka, O., Takikawa, Y., and Kawagoe, R. (2000). Role of the basal ganglia in the control of purposive saccadic eye movements. Physiol Rev *80*, 953-978.

Hofbauer, A., and Drager, U.C. (1985). Depth segregation of retinal ganglion cells projecting to mouse superior colliculus. J Comp Neurol *234*, 465-474.

Humphries, M.D., Khamassi, M., and Gurney, K. (2012). Dopaminergic Control of the Exploration-Exploitation Trade-Off via the Basal Ganglia. Front Neurosci *6*, 9.

Kim, C.K., Ye, L., Jennings, J.H., Pichamoorthy, N., Tang, D.D., Yoo, A.W., Ramakrishnan, C., and Deisseroth, K. (2017). Molecular and Circuit-Dynamical Identification of Top-Down Neural Mechanisms for Restraint of Reward Seeking. Cell *170*, 1013-1027 e1014.

Koike, H., Demars, M.P., Short, J.A., Nabel, E.M., Akbarian, S., Baxter, M.G., and Morishita, H. (2016). Chemogenetic Inactivation of Dorsal Anterior Cingulate Cortex Neurons Disrupts Attentional Behavior in Mouse. Neuropsychopharmacology *41*, 1014-1023.

Krauzlis, R.J., Lovejoy, L.P., and Zenon, A. (2013). Superior colliculus and visual spatial attention. Annu Rev Neurosci *36*, 165-182.

Leinweber, M., Ward, D.R., Sobczak, J.M., Attinger, A., and Keller, G.B. (2017). A Sensorimotor Circuit in Mouse Cortex for Visual Flow Predictions. Neuron *96*, 1204.

Li, N., Chen, T.W., Guo, Z.V., Gerfen, C.R., and Svoboda, K. (2015). A motor cortex circuit for motor planning and movement. Nature *519*, 51-56.

Madisen, L., Garner, A.R., Shimaoka, D., Chuong, A.S., Klapoetke, N.C., Li, L., van der Bourg, A., Niino, Y., Egolf, L., Monetti, C., *et al.* (2015). Transgenic mice for intersectional targeting of neural sensors and effectors with high specificity and performance. Neuron *85*, 942-958.

Miller, E.K., and Cohen, J.D. (2001). An integrative theory of prefrontal cortex function. Annu Rev Neurosci *24*, 167-202.

Moore, T., and Fallah, M. (2001). Control of eye movements and spatial attention. Proc Natl Acad Sci U S A *98*, 1273-1276.

Morcos, A.S., and Harvey, C.D. (2016). History-dependent variability in population dynamics during evidence accumulation in cortex. Nat Neurosci *19*, 1672-1681.

Munoz, D.P., and Everling, S. (2004). Look away: the anti-saccade task and the voluntary control of eye movement. Nat Rev Neurosci *5*, 218-228.

Murugan, M., Jang, H.J., Park, M., Miller, E.M., Cox, J., Taliaferro, J.P., Parker, N.F., Bhave, V., Hur, H., Liang, Y., *et al.* (2017). Combined Social and Spatial Coding in a Descending Projection from the Prefrontal Cortex. Cell *171*, 1663-1677 e1616.

Otis, J.M., Namboodiri, V.M., Matan, A.M., Voets, E.S., Mohorn, E.P., Kosyk, O., McHenry, J.A., Robinson, J.E., Resendez, S.L., Rossi, M.A., *et al.* (2017). Prefrontal cortex output circuits guide reward seeking through divergent cue encoding. Nature *543*, 103-107.

Panzeri, S., Harvey, C.D., Piasini, E., Latham, P.E., and Fellin, T. (2017). Cracking the Neural Code for Sensory Perception by Combining Statistics, Intervention, and Behavior. Neuron *93*, 491-507.

Pinto, L., and Dan, Y. (2015). Cell-Type-Specific Activity in Prefrontal Cortex during Goal-Directed Behavior. Neuron *87*, 437-450.

Raposo, D., Kaufman, M.T., and Churchland, A.K. (2014). A category-free neural population supports evolving demands during decision-making. Nat Neurosci *17*, 1784-1792.

Raymond, C.S., and Soriano, P. (2007). High-efficiency FLP and PhiC31 site-specific recombination in mammalian cells. PLoS One *2*, e162.

Robinson, D.A. (1972). Eye movements evoked by collicular stimulation in the alert monkey. Vision Res *12*, 1795-1808.

Rozeske, R.R., Jercog, D., Karalis, N., Chaudun, F., Khoder, S., Girard, D., Winke, N., and Herry, C. (2018). Prefrontal-Periaqueductal Gray-Projecting Neurons Mediate Context Fear Discrimination. Neuron *97*, 898-910 e896.

Sanders, J.I., and Kepecs, A. (2012). Choice ball: a response interface for two-choice psychometric discrimination in head-fixed mice. J Neurophysiol *108*, 3416-3423.

Schiller, P.H., Sandell, J.H., and Maunsell, J.H. (1987). The effect of frontal eye field and superior colliculus lesions on saccadic latencies in the rhesus monkey. J Neurophysiol *57*, 1033-1049.

Shenhav, A., Cohen, J.D., and Botvinick, M.M. (2016). Dorsal anterior cingulate cortex and the value of control. Nat Neurosci *19*, 1286-1291.

Strang, G. (2016). Introduction to linear algebra, 5 edn (Wellesley, MA: Wellesley-Cambridge Press).

Stubblefield, E.A., Costabile, J.D., and Felsen, G. (2013). Optogenetic investigation of the role of the superior colliculus in orienting movements. Behav Brain Res *255*, 55-63.

Svoboda, K., and Li, N. (2018). Neural mechanisms of movement planning: motor cortex and beyond. Curr Opin Neurobiol *49*, 33-41.

Tallquist, M.D., and Soriano, P. (2000). Epiblast-restricted Cre expression in MORE mice: a tool to distinguish embryonic vs. extra-embryonic gene function. Genesis *26*, 113-115.

Tehovnik, E.J., Slocum, W.M., and Schiller, P.H. (2003). Saccadic eye movements evoked by microstimulation of striate cortex. Eur J Neurosci *17*, 870-878.

Tseng, Q., Wang, I., Duchemin-Pelletier, E., Azioune, A., Carpi, N., Gao, J., Filhol, O., Piel, M., Thery, M., and Balland, M. (2011). A new micropatterning method of soft substrates reveals that different tumorigenic signals can promote or reduce cell contraction levels. Lab Chip *11*, 2231-2240.

Wallace, S.F., Rosenquist, A.C., and Sprague, J.M. (1990). Ibotenic acid lesions of the lateral substantia nigra restore visual orientation behavior in the hemianopic cat. J Comp Neurol *296*, 222-252.

Wang, Q., and Burkhalter, A. (2007). Area map of mouse visual cortex. J Comp Neurol *502*, 339-357.

Wang, Q., and Burkhalter, A. (2013). Stream-related preferences of inputs to the superior colliculus from areas of dorsal and ventral streams of mouse visual cortex. J Neurosci *33*, 1696-1705.

White, M.G., Panicker, M., Mu, C., Carter, A.M., Roberts, B.M., Dharmasri, P.A., and Mathur, B.N. (2018). Anterior Cingulate Cortex Input to the Claustrum Is Required for Top-Down Action Control. Cell Rep *22*, 84-95.

Wickersham, I.R., and Sullivan, H.A. (2015). Rabies viral vectors for monosynaptic tracing and targeted transgene expression in neurons. Cold Spring Harb Protoc *2015*, 375-385.

Wickersham, I.R., Sullivan, H.A., and Seung, H.S. (2010). Production of glycoprotein-deleted rabies viruses for monosynaptic tracing and high-level gene expression in neurons. Nat Protoc *5*, 595-606.

Wimmer, R.D., Schmitt, L.I., Davidson, T.J., Nakajima, M., Deisseroth, K., and Halassa, M.M. (2015). Thalamic control of sensory selection in divided attention. Nature *526*, 705-709.

Wolf, A.B., Lintz, M.J., Costabile, J.D., Thompson, J.A., Stubblefield, E.A., and Felsen, G. (2015). An integrative role for the superior colliculus in selecting targets for movements. J Neurophysiol *114*, 2118-2131.

Ye, L., Allen, W.E., Thompson, K.R., Tian, Q., Hsueh, B., Ramakrishnan, C., Wang, A.C., Jennings, J.H., Adhikari, A., Halpern, C.H., *et al.* (2016). Wiring and Molecular Features of Prefrontal Ensembles Representing Distinct Experiences. Cell *165*, 1776-1788.

Zhang, S., Xu, M., Chang, W.C., Ma, C., Hoang Do, J.P., Jeong, D., Lei, T., Fan, J.L., and Dan, Y. (2016). Organization of long-range inputs and outputs of frontal cortex for top-down control. Nat Neurosci *19*, 1733-1742.

Zhang, S., Xu, M., Kamigaki, T., Hoang Do, J.P., Chang, W.C., Jenvay, S., Miyamichi, K., Luo, L., and Dan, Y. (2014). Selective attention. Long-range and local circuits for top-down modulation of visual cortex processing. Science *345*, 660-665.

Zhao, X., Liu, M., and Cang, J. (2014). Visual cortex modulates the magnitude but not the selectivity of looming-evoked responses in the superior colliculus of awake mice. Neuron *84*, 202-213.

Zingg, B., Chou, X.L., Zhang, Z.G., Mesik, L., Liang, F., Tao, H.W., and Zhang, L.I. (2017). AAV-Mediated Anterograde Transsynaptic Tagging: Mapping Corticocollicular Input-Defined Neural Pathways for Defense Behaviors. Neuron *93*, 33-47.

Acknowledgments

We thank Michael Halassa for thoughtful comments, and Vincent Pham for assistance with histological experiments. This work was supported by grants from National Eye Institute F32 EY024857 to R.H., National Institute of Mental Health K99 MH112855 to R.H., National Eye Institute F32 EY028028 to G.O.S., Natural Sciences and Engineering Research Council of Canada PDF 487824-2016 to V.B.P., National Institute of Mental Health U01 MH106018 and U01 MH109129 to I.R.W., National Eye Institute R01 EY007023 to M.S., National Institute of Neurological Disease and Stroke U01 NS090473 to M.S., National Science Foundation EF1451125 to M.S., and Simons Foundation Autism Research Initiative to M.S.

Author contributions

R.H. and M.S. conceived the project and developed the concepts presented. R.H. designed the experiments and analysis approach with contribution from M.S. R.H. and G.P. designed and implemented the behavioral task. R.H. carried out anatomical, behavioral, optogenetic, and calcium imaging experiments, with contributions from G.O.S. and L.G, and analyzed the data. E.A. developed the linear activity model, with input from R.H. and M.S. V.B.P. performed and analyzed the extracellular recording experiments, with input from R.H. I.C.W. provided unpublished reagents. R.H. and M.S. wrote the manuscript with input from all authors.

Declaration of interests

The authors declare no competing interests.

Data and materials availability

Data and associated code for analysis available upon request from the corresponding author.

Materials and Methods

Animals: All experimental procedures performed on mice were approved by the Massachusetts Institute of Technology Animal Care and Use Committee. Mice were housed on 12 hour light/dark cycle. Animals were group housed before surgery and singly housed afterwards. Adult mice (> 2 months) of either sex were used for these studies. In addition to wild type mice, transgenic lines of the following genotypes were used: PV-Cre (Jackson Laboratory stock # 008069), VGAT-

ChR2-YFP (Jackson Laboratory stock # 014548), Rbp4-Cre (MMMRC stock # 031125), Ai94(TITL-GCaMP6s)-D (Jackson Laboratory stock # 024104), and Ai65(RCFL-tdT)-D (Jackson Laboratory stock # 021875).

Surgical procedures: Surgeries were performed under isoflurane anesthesia (3-4% induction, 1-2.5% maintenance). Animals were given analgesia (slow release buprenex, 0.1mg/kg and Meloxicam 0.1mg/kg) before surgery and their recovery was monitored daily for 72 hours. Once anesthetized, animals were fixed in a stereotaxic frame. The scalp was sterilized with betadine and ethanol. For anatomical tracing experiments, we made a midline incision in the scalp using a scalpel blade. Depending on the experiment, rabies or AAV viruses were injected in the visual cortex (AP: -3.5mm, ML: 2.5mm, DV: 0.5 mm), caudal ACC (AP: 0.3mm, ML: 0.5mm, DV: 0.5 mm), rostral ACC (AP: 1.6mm, ML: 0.3mm, DV: 1.3 mm), or the superior colliculus (at AP: -3.6mm, ML: 1mm, and DV: 1.5mm) using a microinjector (Stoelting). After virus injection, the scalp was reclosed with sutures and skin adhesive (Vetbond).

The following surgical procedures were performed for optogenetics or imaging experiments. For experiments requiring the use of dental acrylic, we removed a portion of the scalp using spring scissors, scraped away the periosteum membrane overlying the skull, and used a dental drill to abrade the skull to improve adhesion. Same animals were used for inactivation of the visual cortex or its projection to the anterior cingulate cortex. We drilled a 3mm craniotomy over the visual cortex and made 8-12 injections (100nL each) of an AAV5.CaMKII.Jaws-KGC-GFP-ER2 (University of North Carolina vector core) virus 0.5mm below the surface in a grid pattern. Injections were centered on the left primary visual cortex (centered at AP: -3.5mm, ML: 2.5mm; range AP: 4 to 3mm, ML: 2.2 to 2.8mm). Craniotomies were fitted with a chronic window, which was assembled from a 3mm coverslip attached to a 5mm coverslip (Warner instruments) with UV curing adhesive (Norland 61). Chronic windows were adhered to the skull using Metabond dental acrylic (Parkell). Visual cortex axons in ACC were photoinhibited through 3mm chronic windows implanted over the ACC (centered at AP: 0.5mm and ML: 0mm, n = 2) or through cannulas (300µm/0.39NA core fiber optic coupled to a 2.5mm stainless steel ferrule; CFMC13L02, Thorlabs) with optic fibers extending 0.3mm below the pial surface (n = 2). For photoinhibition of the ACC, we used either VGAT-ChR2 mice (n = 2) or PV-Cre mice (n = 3) injected with AAV1.EF1.dflox.hChR2(H134R)-mCherry (University of Pennsylvania vector core) at coordinates AP: 0.5mm, ML: 0.5mm, and DV: 0.5 and 1mm (250 nL at each site). PV-Cre mice

were implanted with cannulas such that the optical fiber was 0.3mm below the pia. Fiber optic cannulas were secured on the skull using layers of Metabond and were protected with a dust cap until used for experiments. VGAT-ChR2 mice were implanted with a 3mm chronic window over the ACC. For photoinhibition of the superior colliculus (SC), we injected AAV5-hSyn.Jaws-KGC-GFP-ER2 (100nL) in the intermediate/motor layer (at AP: -3.6mm, ML: 1mm, and DV: 1.5mm) and implanted a fiber optic cannula 0.2mm dorsal to the injection site in wildtype mice (n = 5). For modulating ACC outputs to the superior colliculus, we injected either AAV5-CaMKII-Jaws-KGC-GFP-ER2 (n = 5), or AAV5-CaMKII-eNpHR3.0-EYFP (n = 2) (University of North Carolina vector core) in the ACC of wildtype mice and implanted a fiber optic cannula over the intermediate layer of the superior colliculus (at AP: -3.6mm, ML: 1mm, DV: 1.3mm) on one side of the brain. In a subset of these experiments, AAV5-CaMKII-Jaws-KGC-GFP-ER2 was injected bilaterally in the ACC. One side of the brain was implanted with a chronic window over the visual cortex and the SC on the opposite side was implanted with a fiber optic cannula.

For all imaging experiments in the ACC, we drilled a 3mm craniotomy (at same coordinates as used for optogenetic experiments) and implanted a chronic window assembled from two 3mm coverslips glued to a 5mm coverslip using the UV curable adhesive (double-chronic window). The additional 3mm coverslip was required to minimize movement artifacts for GCaMP recordings during task performance. To label superior colliculus-projecting ACC neurons (ACC-SC), we injected 100nL of red retrobeads (Lumaflour) in the intermediate/motor layer of the SC (at AP: -3.6mm, ML: 1mm, DV: 1.7mm). For axonal imaging experiments, 200nL of AAV1-Syn-GCaMP6-WPRE-SV40 virus was injected unilaterally in the visual cortex (AP: -3.5mm, ML: 2.5 mm, DV: 0.5 mm) or the opposite ACC (AP: 0.5mm, ML: 0.5 mm, DV: 0.5 mm).

To assess the effect of ACC photoactivation on single-unit activity in the SC, 250 nL of AAV5-CaMKII-ChR2 was injected in the ACC at (AP: 0.5mm, ML: 0.5mm, DV: 0.5mm). Depending on the experiment, the fiber optic cannula was implanted either on the same side or opposite to the site of virus injection, with the fiber tip extending 0.3mm below the surface. Stereotaxic location of the SC (AP: -3.6mm, ML: 1mm) was marked on the skull with black ink. The skull was covered with silicone elastomer (Kwik-Cast, World Precision Instruments) to prevent Metabond from adhering to it directly.

For all experiments, after implantation of chronic windows or optic fiber cannulas, the skull was attached to a stainless steel custom-designed head plate (eMachines.com) using Metabond.

Animals were allowed to recover for at least five days before commencing water restriction for behavioral experiments.

Virus-mediated anatomical tracing: Standard histological techniques were used for analysis of retrograde and anterograde transsynaptic tracing experiments and for post-hoc verification of implantation/injection sites. Mice were deeply anesthetized with isofluorane and transcardially perfused with a 4% paraformaldehyde (PFA) solution prepared in phosphate buffered saline (PBS). Extracted brains were postfixed in 4% PFA overnight at 4°C, then kept in PBS until sectioning. Fixed brain tissue was sectioned using a microtome (Leica VT-1000) into coronal slices (thickness of 50-100 µm, depending on the experiment). Slices were stained with DAPI and mounted on glass microslides using Vectashield hardset mounting media. Mounted sections were stored at 4°C until they were imaged using a laser scanning confocal microscope (Leica SP8).

Rabies viral vectors were made as described (Wickersham and Sullivan, 2015). Briefly, HEK 293T cells (ATCC CRL-11268) were transfected with expression vectors for the ribozyme-flanked viral genome (cSPBN-4GFP (Addgene 52487) or pRVΔG-4tdTomato (Addgene 52500)), rabies viral genes (pCAG-B19N (Addgene 59924), pCAG-B19P (Addgene 59925), pCAG-B19G (Addgene 59921), and pCAG-B19L (Addgene 59922)), and the T7 polymerase (pCAG-T7Pol (Addgene 59926)). Supernatants were collected from 4 to 7 days after transfection, filtered, and pooled, passaged 3-4 times on BHK-B19G2 cells (Wickersham et al., 2010) at a multiplicity of infection of 2-5, then passaged on BHK-EnvA2 cells at a multiplicity of infection of 2. Purification, concentration, and titering were done as described.

To make AAV1-CAG-Flpo, the Flpo gene (Raymond and Soriano, 2007) was cloned into pAAV-CAG-FLEX-EGFP (Addgene 59331) to make pAAV-CAG-Flpo. Serotype 1 AAV was produced by triple transfection of HEK 293T cells with pAAV-syn-Flpo, pAAV-RC1, and pHelper (Cellbiolabs VPK-401) (per 15 cm plate, 15.5 ug, 21.0 ug, and 33.4 ug respectively) using Xfect (Clontech 631318) transfection reagent. Supernatants and cells were harvested at 72 hours posttransfection and viruses purified and concentrated by iodixanol gradient centrifugation (Choi et al., 2006).

For quantification of dual-rabies retrograde tracing experiments from caudal and rostral ACC, we sliced the brain into 100 µm section and imaged GFP and/or tdTomato fluorescence from every other slice using a 10x/0.4NA objective (Leica). Anatomical landmarks, such as position/size of ventricles, corpus callosum, striatum, and hippocampus, were used to manually

align slices to a standard mouse brain atlas (Franklin, 2013). Back-labeled cells were counted using the cell counter plugin in ImageJ (NIH). For the results presented in Figure 2C, we counted the number of retrogradely neurons present in the different divisions of the visual cortex and normalized by the total number of GFP- and tdTomato-expressing back-labeled cells found in the posterior cortex (0 to -4.0 mm posterior, relative to Bregma). For quantifying the distribution of cells projecting to the intermediate and deep layers of the SC (Figure S4I), we counted the number of cells found in the ACC as a function of distance from Bregma in 0.5mm bins. Since the sensory and intermediate/motor layers of the superior colliculus are <0.5mm apart, it is challenging to restrict virus injection to the motor layer. However, the frontal cortex predominantly projects only to the motor layer; hence, to minimize contamination from virus spillover into the sensory layer of the superior colliculus, we normalized the number of neurons in the ACC by the total number of back-labeled neurons found in the frontal cortex (0 to +3mm anterior, relative to Bregma).

We injected rabies viruses encoding GFP or tdTomato into the visual cortex or the superior colliculus to identify ACC neurons projecting to these structures. We counted the total number of back-labeled neurons in the ACC (AP range 0 to 1mm), every 200 µm in each animal and quantified the proportion of neurons that were labeled with GFP, tdTomato, or both out of all labeled cells.

We performed anterograde transsynaptic tracing experiments (Zingg et al., 2017) to identify SC neurons that receive inputs from the ACC. We produced the Flp-dependent tdTomato reporter line Ai65F by crossing the Cre- and Flp- dependent tdTomato double-reporter line Ai65D (Madisen et al., 2015) (Jackson Laboratory 021875) to the Cre deleter line Meox2-Cre (Tallquist and Soriano, 2000) (Jackson Laboratory 003755), so that only Flp is required for expression of tdTomato. An AAV1-CAG-Flpo virus was injected in the ACC of these mice to label postsynaptic neurons with tdTomato. After allowing 4-6 weeks for tdTomato expression, we sectioned the brain into 50µm slices and used standard immunohistochemistry techniques to identify GABA-expressing neurons co-labeled with tdTomato. The tissue was placed in 5% normal goat serum, 1% triton blocking solution in 0.1M phosphate buffered saline (PBS) for 1 hour at room temperature. It was then incubated in primary antibody against GABA (rabbit anti-GABA, 1:500, A2052 Sigma) and 1% NGS/ 0.5% triton overnight at 4ºC. Following washing in 0.1M PBS 3x10’, the tissue was incubated in secondary antibody (goat anti-rabbit IgG AlexaFluor 488, 1:500, Invitrogen) and 1% NGS for 4 hours at room temperature. Tissue was then washed 3x10’ in PBS,

mounted, and coverslipped with anti-fade mounting medium (Prolong Gold, ThermoFisher). Tiled z-stacks were collected on a confocal microscope (SP8, Leica) using a 20x objective at 1024x1024 resolution, 2 µm apart (~20 z-slices) from sections containing the SC (between -3.4 and -4.7 AP from bregma). We counted the total number of tdTomato-labeled cells in the SC and quantified the proportion of these neurons that were also positive for GABA (Cell counter plugin).

Behavioral apparatus and training: Mice were trained to report the spatial location of visual stimuli by rotating a trackball left or right with their forepaws, similar to a previously described design (Sanders and Kepecs, 2012). Animals were headfixed on a behavior rig assembled from optical hardware (Thorlabs), placed in a polypropylene tube to limit body movement, and positioned ~8 cm from an LCD screen (7" diagonal; 700YV, Xenarc Direct) such that their forepaws rest on a trackball. Ball movements were monitored with a commercially available USB optical trackball mouse (Kensington Expert Mouse K64325). The original trackball was replaced with a 55mm diameter ping pong ball (Joola), which was light enough for mice to rotate comfortably. We inserted a hypodermic tube down the center of the trackball so it could only be rotated along a single axis (left or right). To fix the ping pong ball to the optical mouse, we made grooves in the trackball chassis and secured the hypodermic needle with hot glue. A USB host shield (SainSmart) was used to connect the output of the optical mouse to a microcontroller (Arduino), which ran a custom routine that detected ball movements every 10ms. In the event of a ball movement, the microcontroller outputted a timestamp and the amount of movement (in pixels) to a behavioral control computer running Windows XP (Dell). In addition, a time stamp was sent every 100ms to synchronize timing between the microcontroller and the behavior computer. In our system, one pixel of optical mouse movement corresponded to ~0.15º movement on the ball. Behavioral control was implemented with custom software written in MATLAB (Mathworks) using the Psyhcophysics and the Data Acquistion toolboxes. On each trial, the presented visual cue (black square, ~20º) started on either the left or the right side of the LCD screen. The trackball controlled the location of the visual stimulus in closed-loop in real-time. The gain of coupling between the trackball and the stimulus was calibrated so that rotating the ball by the threshold amount (15º) in the correct direction moved the stimulus from its starting position to the center of the screen. Ball positions were accumulated throughout the trial until the stimulus reached the center or the response window expired. Under this closed-loop control, any movement in the incorrect direction displaced the stimulus farther away from the center and towards the edge of the screen. Hence,

such movements had to be offset by additional movement in the correct direction for the stimulus to move to the center of the screen and for the trial to be considered correct. If the ball was moved opposite to the direction of the instructed cue by the threshold amount, the stimulus moved to the edge of screen and the trial was considered incorrect. Water reward was delivered through a metal spout placed within the reach of the tongue on correct trials; the amount dispensed was controlled by opening a solenoid valve for a calibrated period of time.

Mice were taken through successive stages of training until they became proficient at the task. Once mice recovered from the surgery, they were water restricted for 5-7 days (≥ 1ml/day) and then trained to lick the metal spout to obtain small water rewards (3-6 μL). If mice did not receive their water allotment during training, they were given the remaining amount as hydrogel (Clear H_2O) in their home cage. After mice reliably licked the water spout, they earned water rewards by using the trackball to move the presented stimulus to the center of the screen. To discourage spontaneous trackball movements, mice were required to hold the ball still for 1s to trigger trial start, which was signaled with an auditory tone (0.5s, 1 KHz); the visual cue appeared with a 1s delay after trial start. During early stages of training, only movements in the correct direction contributed to movement of the stimulus. Once mice reliably moved the ball in either direction on >90% of trials, this condition was removed and the movement of the stimulus was fully coupled to the movement of the trackball. In the next stage of training, we used an anti-bias algorithm in which the same stimulus was repeated on consecutive trials if mice made an error until they performed the trial correctly; stimulus location on trials following correct trials were randomly chosen. Once performance reached 70%, the anti-bias algorithm was turned off and stimuli were presented in a randomized manner. Throughout all stages, white noise was used to signal miss trials if mice failed to move the ball to threshold before expiration of the response window. As mice progressed through the training stages, we gradually decreased the response time from 10s to 1-2s. Correct and incorrect trials were signaled with an auditory tone (0.2 kHz and 10kHz, respectively), followed by an inter-trial delay of 2.5s. In a subset of mice, incorrect trials were punished with a brief timeout (3s), lengthening the inter-trial delay to 5.5s.

Animals trained for two-photon imaging experiments were taken through two additional stages of training. First, we turned off the closed-loop coupling between the trackball and the stimulus, and flashed stimuli for 100-200ms. Second, we introduced uncertainty in temporal expectancy for stimulus onset by randomizing the period (exponential distribution with mean of

~1.8 seconds, min and max delay of 1 and 5s, respectively) between the auditory cue signaling trial start and the onset of the visual stimulus. Once animals achieved criterion performance of 70% correct with randomized trials, we commenced optogenetic or imaging experiments.

We also trained a subset of mice on two variants of the task to interrogate their psychometric performance. In the first variant, we presented a single visual cue as before but of varying luminance values. In the second variant, mice were presented with two cues simultaneously (target and distractor). Stimuli were flashed for 200-400ms and the closed-loop coupling between trackball movements and the stimulus location was turned off. The luminance of the target cue was set to 64% while that of the distractor cue ranged from 0 to 48%; animals were rewarded for selecting the target cue with appropriate trackball movement. We quantified performance (excluding miss trials) for each target-distractor stimulus pair to assess the effect of perceptual ambiguity on action selection in the task.

Behavioral analysis: We computed several metrics to quantify performance for each trial type on individual behavioral sessions. The error rate was the proportion of trials in which the ball was moved opposite the direction instructed by the cue out of all completed trials for each visual stimulus (i.e., excluding miss trials). The miss rate was the proportion of trials in which the ball was not moved to threshold out of all trials where a given stimulus was presented. The response window was set to 1s for most animals. However, imposing this restriction on some mice led to a high miss rate and a response window of 2s was used instead. The movement start time and movement velocity was calculated using kinematic analysis of movement trajectories. The microcontroller counted the number of pixels the ball was moved in each 10ms time bin. A trace of ball position vs. time from stimulus onset was constructed by taking a cumulative sum of these pixel counts and scaling by 0.15º/pixel. The resulting trace was resampled at 100Hz using the 'interp1' function in MATLAB. Next, we computed instantaneous velocity and acceleration traces by computing the first and second time derivatives of the position trace. Movement start was defined as the first time point when the absolute value of the instantaneous acceleration exceeded a threshold value and the absolute value of the ball position was greater than 0.75º. The acceleration threshold value was optimized manually so that the algorithm picked start times preceding smooth and continuous movements, ignored spurious movements, and performed well across different animals. Robustness of this kinematic analysis was verified by visual inspection of position traces marked with the movement start times picked by the algorithm. Mean

instantaneous velocity for each trial was then calculated by averaging the instantaneous velocity values between the movement start time and the time at which the ball position reached the threshold.

Optogenetic manipulation of behavior: Photostimulation was provided with a solid state 473nm blue laser for experiments using ChR2 and a 593nm yellow laser for experiments using Jaws or eNpHR3.0 (OptoEngine). Laser stimulation was triggered from the behavior control computer and lasted from 0.3s before to 1s after visual cue onset. 15-20% of trials were pseudorandomly selected for photostimulation. We additionally imposed the condition that photostimulation could not occur on two consecutive trials. The output of the laser was coupled to a 300µm core/0.39NA patch cable (Thorlabs) with a FC/PC fiber coupler (OptoEngine). Laser power through the patch cable was measured with a digital power meter before each experiment (Thorlabs). In experiments requiring photostimulation through chronic windows over the visual cortex, the ceramic ferrule of the patch cable was positioned so it filled the entire 3mm window and delivered a constant light pulse with 20mW of power. Since the ACC is a midline structure and the chronic window was implanted such that it exposed both hemispheres, we placed a light obstructing material (Mounting Putty, Scotch) over one hemisphere and positioned the patch cable ferrule so it illuminated a ~1mm spot over the targeted hemisphere. In experiments requiring light delivery through implanted optical fiber, the ceramic ferrule of the patch cable was coupled to the fiber optic cannula with a ferrule mating sleeve (ADAF1, Thorlabs). Constant blue (10-20mW) or yellow (20mW) light was used for photostimulation of inhibitory neurons or visual cortex axons in the ACC, respectively. Activity in the superior colliculus was inhibited by delivering 5-10mW of constant yellow light. Photoinhibition of ACC outputs was achieved by constant yellow light (20mW) illumination through an implanted fiber optic cannula (SC) or through a chronic window (VC).

Trials were labeled as ipsi or contra depending on the location of the presented cue relative to the site of photostimulation. For each experiment, we analyzed the first three sessions with photostimulation in which the performance on non-laser trials for both trial-types was at least 60% correct. In each session, we computed the error rate and the miss rate on ipsi and contra trials separately for laser and non-laser trials. The effect of photostimulation on behavioral performance was quantified by comparing the error rate between laser-on and laser-off conditions. We similarly quantified the effect of photostimulation on movement start times and movement velocity.

We computed contra action bias as the percentage of trials in which the animal made contra movements out of all completed trials (i.e., excluding miss trials) regardless of the stimulus presented. Although stimulus presentations were randomized, individual sessions could have uneven number of contralateral and ipsilateral stimulus trials. Moreover, the miss rate for the two trial types may not necessarily be the same. To account for these issues, we subsampled an equal number of non-miss contralateral and ipsilateral stimulus trials (5 trials each) and calculated the proportion of trials in which the animal selected the contra action separately for laser and non-laser trials. This process was repeated 1000 times for each session. The contra action bias rate for laser and non-laser trials on each session was then estimated by averaging these 1000 values. The effect of photostimulation was determined by calculating the laser-induced normalized change in contra action bias using the following equation:

$$\frac{ContraBias_{laser} - ContraBias_{nonlaser}}{ContraBias_{nonlaser}}$$

This value reflects the degree to which photostimulation changes the contra action bias relative to performance on non-laser trials.

Population statistics were derived by pooling individual sessions across all animals and comparisons were made using the Wilcoxon signed-rank test (two-sided). Since analyses that compared the effect of photostimulation on contra and ipsi stimulus trials tested two hypotheses, we determined significance using the Bonferroni adjusted p-value of 0.05/2 = 0.025. We also used the signed-rank test to determine if the laser-induced normalized change in contra action bias was from different from zero.

Two-photon microscopy: GCaMP6s fluorescence was imaged through a 16x/0.8 NA objective (Nikon) using galvo-galvo scanning with a Prairie Ultima IV two-photon microscopy system. Excitation light at 910nm was provided by a tunable Ti:Sapphire laser (Mai-Tai eHP, Spectra-Physics) equipped with dispersion compensation (DeepSee, Spectra-Physics). Emitted light was collected with GaAsP photomultiplier tubes (Hamamatsu). A blackout curtain attached to a custom stainless steel plate (eMachineShop.com) was mounted on the headplate to prevent light from the LCD screen from entering the PMTs. Layer 5 GCaMP6s-expressing neurons in transgenic animals were imaged with 2x optical zoom, 350-550µm below the brain surface for 20-minute-long behavioral sessions. Upon completion, excitation wavelength was changed to 830nm, which produced both a signal from the retrobeads and a structural green signal from GCaMP6. Emission

signals were split with a dichroic mirror (FF649-Di01; Semrock) mounted in a filter cube and directed to two different PMTs. Simultaneous imaging of both signals with 830nm excitation facilitated spatial alignment of retrobead signals to GCaMP6s signals collected during behavior and allowed us to identify SC-projecting ACC neurons (see 'Image analysis'). 4x optical zoom was used for imaging callosal or visual cortex axons in the ACC up to 100µm below the surface. All imaging experiments were performed at a frame rate of 5Hz. Laser power at the specimen was controlled with pockel cells and ranged from 10 to 50 mW, depending on GCaMP6 expression levels and depth.

Image analysis: Images were acquired using the PrairieView software (Bruker) and saved as multipage TIFF files. Image processing and region of interest (ROI) selection was performed in ImageJ (NIH). To correct for lateralized movements in the x-y axis, images were realigned to a reference frame (the pixel-wise mean of all frames) using the template matching plugin (Tseng et al., 2011). ROIs were drawn manually over visually identified neurons on reference frames generated by taking the pixel-wise maximum, mean, and standard deviation of all frames. For each neuron, the same shaped ROI was also placed in an adjacent area devoid of other neurons to estimate the background neuropil signal. To minimize the contribution of the neuropil signal to the somatic signal, corrected neuronal fluorescence time series was estimated as $F(t) = F_{raw_soma}(t) - 0.7 \times F_{raw_neuropil}(t)$ (Chen et al., 2013). Similar image analysis was used for axonal imaging experiments, except ROIs were drawn over visually-identified boutons and fluorescence signals were not adjusted for neuropil contamination. $\Delta F/F$ (DFF) for each neuron or bouton was calculated as $\Delta F/F(t) = 100 \times (F(t) - F_0)/F_0$, where F_0 was the estimated mode of the distribution of raw fluorescence values.

To identify retrobead-containing neurons, a reference frame was generated by taking the pixel-wise mean of realigned GCaMP6s frames acquired during the behavioral session. The green channel acquired with excitation at 830nm was realigned to this reference using the template matching plugin. The resulting translation values were then applied to the channel containing signals from retrobeads. An average projection was taken after this realignment and superimposed onto the reference frame used for drawing ROIs. Neurons containing retrobeads were then visually identified.

Analysis of task responses of ACC neurons: For imaging experiments, trials were labeled contra or ipsi depending on the location of the visual cue relative to the hemisphere imaged. DFF

responses on each trial were aligned by stimulus onset and correct contra/ipsi trials were sorted into separate groups. The mean DFF activity averaged over a 1s pre-stimulus and 1s post-stimulus period was compared using the Wilcoxon signed-rank test. Neurons with significantly higher activity after stimulus onset ($p < 0.05$, one-sided) on either trial type were considered task-modulated.

To facilitate population comparisons, DFF signals were z-score normalized with baseline activity over a 1s pre-stimulus period. AUROC values were computed for each task-modulated neuron by comparing the z-scored activity (averaged over a 1s period after stimulus onset) on correct contra and ipsi trials. A trial preference score was then computed as 2 x (AUROC – 0.5); this score ranged from 1 (complete contra preference) to -1 (complete ipsi preference). To determine if individual task-modulated neurons had significant trial preference, scores were recomputed after shuffling trial labels 1000 times. Observed preference scores outside the center 95% of the shuffled distribution were considered significant ($p < 0.05$, two-sided).

We assayed the visual responsiveness of visual cortex or callosal axons in the ACC in animals passively viewing visual stimuli presented at the same locations as during the task (solid black square for visual cortex axons, gratings drifting at 90º for callosal axons; 1s stimulus duration). Visually responsive boutons were identified by comparing pre-stimulus activity averaged over a 1s period to averaged activity 0.6s-1.2s after stimulus onset (two-sided Wilcoxon signed-rank test, $p < 0.01$). Stimulus preference scores for visually-responsive boutons were computed using the AUROC analysis, similarly to that described above.

<u>Cue and movement decoding:</u> We built linear support vector machine (SVM) classifiers using the LIBSVM library for MATLAB (Chang, 2011) to probe whether neuronal responses represent information about the location of the visual cue or the direction of the action selected. Selection of the regularization parameter C was performed with a dataset not included in the analysis. We tested a range of values for C and selected the one which gave the best classifier accuracy on an 8-fold cross-validated dataset ($C = 0.4665$). For this procedure, the classifier was trained to distinguish between correct contra and ipsi trials. Neurons in this dataset were simultaneously recorded; however, we only included the minimum number of neurons and trials used in the final decoder for the analysis presented here (see below).

We define the term 'information' here operationally as the prediction accuracy of the trained classifiers (Panzeri et al., 2017). We reasoned that neurons that encode cue information would

respond similarly on trials in which the same cue is presented regardless of the direction of the action chosen on that trial. Similarly, a neuron that encodes movement direction would be active on trials in which a particular movement was chosen regardless of the cue presented. Hence, we used a combination of correct and error trials to train classifiers for decoding cue and movement information (see schematic in Figure 4E). We trained these decoders with responses of each of the following four types of neurons: 1) contra-preferring, unlabeled; 2) contra-preferring, ACC-SC; 3) ipsi-preferring, unlabeled; 4) ipsi-preferring, ACC-SC.

Since we simultaneously recorded only a few cells in each of these groups, we constructed 'pseudotrials' by combining neuronal responses recorded across different sessions with at least 5 error trials for each cue type. There was an unequal distribution of neurons across groups. Hence, we used subsampling so that the same number of neurons were used for training each type of classifier (23 neurons, limited by the number of ipsi-preferring ACC-SC neurons). We also had unequal number of trials between conditions and similarly used subsampling to balance trial types (5 trials for each type). To estimate the predictive power of our classifiers, we ran 1000 iterations of cue and movement decoders separately trained with the z-scored activity (averaged over 1s after stimulus onset) of each of the four types of neurons. A random set of neurons and trials were subsampled on each iteration of the model. We minimized model over-fitting by using the cross validation technique (8-fold) to split the data into a training and testing set on each iteration and estimated classifier performance by averaging the prediction accuracy across the 8 splits. By the end of this procedure, we had 1000 prediction accuracies for each cue/movement decoder trained with the activity of the four different neuron types. We used bootstrapping (subsampling with replacement, 1000 iterations) to calculate a 95% confidence interval for the prediction accuracy of each decoder. To determine if individual decoders performed above chance, we used an identical procedure except that we shuffled the labels for the test data. Mean prediction accuracy (averaged across the 1000 models) derived from correctly labeled test data and falling outside the center 99% of the shuffled distribution were considered significant. To determine if specific neuron types contain different cue and movement information, we compared the corresponding distribution of prediction accuracies using a Wilcoxon rank-sum test (Armstrong et al., 2009). Since this experiment potentially tested 28 different hypotheses (i.e., two types of decoders for four neuron types), we tested significance at the Bonferoni adjusted p-value of 0.01/28 ($\sim 10^{-5}$).

Electrophysiological recordings in the SC: We tested the effect of photostimulating ChR2-expressing callosal input axons or directly activating ChR2-expressing cell bodies on activity in the SC. One or two days before the experiments, mice were habituated to head-fixation in 1h sessions. On the day of the experiment, mice were anesthetized with isoflurane and the Metabond and silicone elastomer on the skull were removed. The mouse was placed on the stereotaxic frame and a 500 μm diameter craniotomy was performed on top of the recording site (from bregma: -3.6 to -4 mm anteroposterior and 0.8 to 1 mm mediolateral). The dura above the cortex was removed and the craniotomy was protected with saline and a piece of gelfoam. The side of the craniotomy depended on the experiment, but was always made ipsilateral to the ACC hemisphere in which the fiber optic cannula was implanted. The skull was covered again with silicone elastomer and the animal was returned to its home cage to recover from anesthesia for at least 2 hours. After recovery, mice were headfixed and the silicone and gelfoam overlaying the craniotomy was gently removed. 0.9% NaCl solution was used to keep the surface of the brain wet for the duration of the recordings.

After placing the animal in the recording set up, we submerged a reference silver wire in the NaCl solution on the skull surface. The position of the 16-channel silicone probe (A1x16-Poly2-5mm-50s-177-A16, NeuroNexus) was referenced on lambda and the surface of the brain and lowered slowly (1 min per mm) to reach superficial sensory layer of the superior colliculus (~1.3 mm in the ventral axis) using a motorized micromanipulator (MP – 285; Sutter Instrument Company). The extracellular signal was amplified using a 1x gain headstage (model E2a; Plexon) connected to a 50x preamp (PBX-247; Plexon) and digitalized at 50 kHz. The signal was highpass filtered at 300Hz. Once the visual layer of the SC was identified (characterized by strong and reliable visual responses to drifting gratings and sparse noise), the recording probe was lowered ~400 μm deeper to the motor layer of the SC. For successful recordings, the silicone probe was gently retracted and the recording tract was marked by re-entering the DiI coated probe (2 mg/mL – D3911, ThermoFisher Scientific) at the same location. For some experiments, we were able to record from two locations spaced 500μm apart in the dorsal-ventral axis. The brain was harvested post-hoc and sectioned to confirm the probe location and ChR2 expression in the ACC. Spikes were isolated online with amplitude threshold using Plexon Recorder software, but re-sorted using the MountainSort automated spike sorting algorithm (Chung et al., 2017). Units were curated manually after automatic detection.

Visual stimuli were presented during recordings in the SC to increase neuronal responsiveness. Sparse noise on a 3 x 5 grid (square size was the same as used for behavior experiments) of black and white square on a gray background (50% luminance) were displayed for 0.1s, followed by a 0.1s gray screen period. Positions were randomized within each block such that black and white squares were presented once at each of the 15 positions. The total duration of a block was 6 sec, with 1s inter-block intervals. Photostimulation of the ACC (10ms blue light pulses at 20 Hz) was performed on 50% of the blocks and lasted throughout the block.

Since ACC axons in the SC target the intermediate and deep layers, we focused our analysis on recordings made from these areas. While we observed robust retinotopically organized visual responses in the superficial layer, we rarely encountered cells in the deeper layers that responded to the sparse noise stimuli presented at specific locations. Therefore, recordings from deeper neurons likely reflect ongoing, spontaneous activity but we cannot rule that the visual stimulation modulated this tonic level of activity. We first determined if individual neurons were significantly modulated by laser activation of the ACC by comparing the firing rates (FR) of activity on non-laser and laser trials. For each modulated neuron, we computed a laser modulation index using the following equation:

$$\frac{FR_{Laser} - FR_{nonlaser}}{FR_{Laser} + FR_{nonlaser}}$$

To test if photostimulation increased or decreased activity in the SC, we tested if the population laser modulation index was significantly different from zero. We also compared the laser modulation observed with direct photoactivation of ACC cell bodies or activation of callosal input axons. All comparisons were made using either two-sided Wilcoxon rank-sum (unpaired) or signed-rank (paired) tests.

<u>Linear activity model:</u> Causal activity manipulation optogenetic experiments aim to understand how specific circuits contribute to behavioral performance, and can be used to formally derive the contributions of distinct pathways to behavior. An anatomically-inspired linear activity model was used to predict how the ACC-VC projection contributes to task performance by modulating activity in SC_m (Figure S10). In this description, we assume that the left side of the brain was inactivated; contralateral/ipsilateral stimuli are designated relative to the inactivated side. Activity in SC_L (the inactivated side) and SC_R was expressed as the linear sum of inputs from four excitatory

pathways: 1) direct ACC-SC pathway that excites the SC on contra trials ($E_{ACC\text{-}SC}$); 2) direct ACC-SC pathway that inhibits the SC on ipsi trials ($I_{ACC\text{-}SC}$); 3) ACC-VC pathway that excites the SC on contra trials ($E_{ACC\text{-}VC\text{-}SC}$), and 4) a default pathway representing the baseline, task-independent activity of the SC (D) (Figure S10A). Pathways 1 and 2 are based on our experiments showing that direct or callosal photoactivation in the ACC increases or decreases activity in the SC, respectively (Figure 3A-D; S7). Pathway 3 is based on previous experiments showing that VC activity is modulated by inputs from the ACC (Leinweber et al., 2017; Zhang et al., 2014) and that the VC in turn modulates activity in the superficial SC (Zhao et al., 2014). We included the non-specific input pathway to account for the baseline activity of SC_m driven by diverse inputs.

We parameterized the contribution of the ACC-SC and ACC-VC-SC pathways by variables c and i, representing the drive provided by the ACC on contra and ipsi trials, respectively. We set these variables based on the observed proportion of ACC-SC neurons preferentially active on correct contra and ipsi cue trials, respectively ($c = 0.65$ and $i = 0.35$, Figure 4D). Importantly, we tested a range of values for these parameters and obtained similar predictions. We defined two equations that express activity in the left and right SC_m for each type of trial (contra or ipsi). Only equations for contra trial are shown as an example, but equations for ipsi trials are defined similarly and obtained by substituting c with i:

$$SC_L(c) = cE_{ACC\text{-}SC} - (1 - c)I_{ACC\text{-}SC} + cE_{ACC\text{-}VC\text{-}SC} + D$$
$$SC_R(c) = (1-c)E_{ACC\text{-}SC} - cI_{ACC\text{-}SC} + (1 - c)E_{ACC\text{-}VC\text{-}SC} + D$$

We defined x as a column vector containing the contribution of each of the four input pathways to activity in SC_L and SC_R

$$x = \begin{bmatrix} E_{ACC-SC} \\ I_{ACC-SC} \\ E_{ACC-VC} \\ D \end{bmatrix}$$

and expressed the equations in matrix form (example for contra trial shown):

$$\begin{bmatrix} SC_L(c) \\ SC_R(c) \end{bmatrix} = \begin{bmatrix} c & -(1-c) & c & 1 \\ 1-c & -c & 1-c & 1 \end{bmatrix} x$$

This matrix determines the activity in each SC_m in the absence of any optogenetic perturbation. The optogenetic inhibition of specific areas or anatomical projections is modeled by substituting the corresponding terms in the above matrix by zeros (see example in Figure S10C, eq. 3). Matrices

for three crucial inactivation experiments considered in the model (of the ACC-SC, ACC, and SC_m) are given below for contra trials. The first and second row in each represents SC_L and SC_R, respectively, for contra trials:

$$\text{ACC-SC: } \begin{bmatrix} 0 & 0 & c & 1 \\ 1-c & -c & 1-c & 1 \end{bmatrix}$$

$$\text{ACC: } \begin{bmatrix} 0 & 0 & 0 & 1 \\ 1-c & 0 & 1-c & 1 \end{bmatrix}$$

$$\text{SC: } \begin{bmatrix} 0 & 0 & 0 & 0 \\ 1-c & -c & 1-c & 1 \end{bmatrix}$$

We assume that behavioral performance on each trial-type is given by the differences $SC_L(c) - SC_R(c)$ and $SC_R(i) - SC_L(i)$, respectively, such that the SC_m hemisphere with the higher level of activity leads to its preferred contra movement. Each of the three experiments, in addition to the control experiment, then yields two linear functions of x, one for contra trials and one for ipsi trials, totaling eight functions. We expressed these functions in matrix form to derive an 8-by-4 matrix A (Figure S10C, eq. 4) that multiplied by vector x describes the behavioral performance ($\boldsymbol{b}$) observed during control and optogenetic experiments (i.e., $Ax = \boldsymbol{b}$, Figure S10C).

Our goal in formulating this linear model is to make a prediction about the contribution of the ACC-VC pathway to behavioral performance that is constrained by the behavioral deficits observed by inactivating the ACC, SC, and ACC-SC pathway. The model, described by the relationship $Ax = \boldsymbol{b}$, posits that optogenetic inactivation experiments cause the observed changes in behavioral performance by perturbing activity in SC_m through the four input pathways represented in x. Hence, we can use this relationship to estimate how activity along pathways represented in x must change to cause the observed changes in behavioral performance. Once we obtain an estimate for x, we can simulate the inactivation of any pathway included in the model (such as the ACC-VC pathway, Figure S10D, eq. 5) and predict how behavioral performance should change if the pathway is experimentally perturbed (see details below).

In $Ax = \boldsymbol{b}$, the behavioral performance vector $\boldsymbol{b}$ aggregates the performance observed during control and the three inactivation experiments. Using this aggregate vector provides only a single estimate of x. In contrast, decomposing $\boldsymbol{b}$ into its four components (represented by b_j, three of which correspond to the change in behavioral performance caused by the inactivation experiments) would allow us to derive separate estimates of x (x_j) from each experiment and hence

a prediction from each of these estimates. We reasoned that comparing predictions derived from separately estimated x_j would allow us to determine their robustness, which would not be possible if we derive only a single estimate by using the non-decomposed vector $\boldsymbol{b}$. Hence, we devised a strategy to make experiment-specific predictions.

Our optogenetic experiments include both regional and axonal inactivation experiments. An important technical consideration is that the extent of inhibition of an area's output achieved by regional or axonal optogenetics may not be equivalent. Likewise, behavioral deficits caused by these manipulations may not be equivalent. We resolved this issue by scaling the observed changes in behavioral performance b_j in each experiment by a positive coefficient that accounts for the reliability of the inactivation method used (w_j). An important consequence of expressing behavioral performance in this way is that it allows us to decompose $\boldsymbol{b}$ into its components. We defined the behavioral performance vector $\boldsymbol{b}$ by a control performance vector $b_{control}$ (all entries in $b_{control}$ are 1, denoting baseline behavioral performance) from which the change in error rate observed on each optogenetic experiment is subtracted. Specifically, $\boldsymbol{b} = w_{control}b_{control} - w_{ACC-SC}b_{ACC-SC} - w_{ACC}b_{ACC} - w_{SC}b_{SC}$, where each w_j is a fixed non-negative scalar and $b_{ACC\text{-}SC}$, b_{ACC}, and b_{SC} are the following vectors:

$$b_{ACC\text{-}SC} = \begin{bmatrix} 0 \\ 0 \\ err^{c}_{ACC-SC} \\ err^{i}_{ACC-SC} \\ 0 \\ 0 \\ 0 \\ 0 \end{bmatrix} \quad b_{ACC} = \begin{bmatrix} 0 \\ 0 \\ 0 \\ 0 \\ err^{c}_{ACC} \\ err^{i}_{ACC} \\ 0 \\ 0 \end{bmatrix} \quad b_{SC} = \begin{bmatrix} 0 \\ 0 \\ 0 \\ 0 \\ 0 \\ 0 \\ err^{c}_{SC} \\ err^{i}_{SC} \end{bmatrix}$$

The term err in these vectors is the laser-induced change in the error rate (i.e., error rate$_{laser}$ – error rate$_{nonlaser}$), with subscript and superscript denoting the experiment and the trial-type, respectively.

We derived experiment-dependent estimates by defining the following system of equations for each of the three experiments: $Ax_{ACC-SC} = b_{ACC-SC}$, $Ax_{ACC} = b_{ACC}$, and $Ax_{SC} = b_{SC}$, where each x_j is the contribution of the four input pathways to activity in the SC as derived from the corresponding optogenetic experiment. Each linear system defined by $Ax_j = b_j$ has more equations than variables and, generally, does not have a unique solution. Hence, we derived estimates $\hat{x}_j$ that best approximate the relationship $A\hat{x}_j = b_j$ by minimizing the squared Euclidean distance $\|A\hat{x}_j -$

b_j ||^2. The optimal $\hat{x}_j$ estimated from each optogenetic experiment is given by least-squares approximation (Strang, 2016), defined generically as $\hat{x}_j = (A^TA)^{-1}A^Tb_j$. Note that all rows except the two corresponding to the specific experiment considered in each experiment-specific b_j are set to 0 (i.e., no change in behavioral performance). Hence, each estimate $\hat{x}_j$ is interpreted as the change in activity along the four inputs to SC_m that is required to best approximate the change in behavioral performance caused by the corresponding inactivation experiment, relative to the activity that would cause no change in behavioral performance. For instance, the estimate $\hat{x}_{SC}$ shows that the decrease in contra bias observed by inactivating the SC in the model is best explained if the D pathway normally contributes significant excitation to the SC. Inhibiting this input through optogenetic inactivation of the left SC reduces activity in SC_L, hence causing the observed decrease in contra bias.

We used each estimated $\hat{x}_j$ to predict the effect of inactivating the ACC-VC pathway on behavior. We simulated the inactivation of the left ACC-VC projection in the model by nulling the contribution of $E_{ACC\text{-}VC\text{-}SC}$ in eq 1. shown in Figure S10A, defining the following matrix:

$$\begin{bmatrix} c & -(1-c) & 0 & 1 \\ 1-c & -c & 1-c & 1 \end{bmatrix}$$

From this matrix, we derived a 2-by-4 matrix P whose first and second row correspond to SC_L(c) $-$ SC_R(c) and $SC_R(i)$ $-$ $SC_L(i)$, as done for making the matrix A (Figure S10D). Using the $\hat{x}_j = (A^TA)^{-1}A^Tb_j$ relationship defined above, we reasoned that the predicted change in behavioral performance during ACC-VC inactivation, $b_{j\text{-}pred}$, for each estimated $\hat{x}_j$ is given by $P\hat{x}_i = b_{j\text{-}pred}$. Hence, by substituting for $\hat{x}_j$, we defined $b_{j\text{-}pred} = P(A^TA)^{-1}A^Tb_j$. The variables c and i in A represent the drive provided by the ACC on contra and ipsi trials, respectively. We set these variables based on the observed proportion of ACC-SC neurons preferentially active on correct contra and ipsi cue trials, respectively (c = 0.65 and i = 0.35; Figure 4D) and calculated $b_{j\text{-}pred}$ for all three experiments. We found that each of the three experiments predicted that inactivating the $E_{ACC\text{-}VC\text{-}SC}$ pathway in the model leads to a decrease in contra actions. Thus, by aggregating the experimental data regardless of their reliability, our analysis predicts that experimentally inactivating the ACC-VC pathway should decrease the selection of contra actions.